Journal Pre-proof

Microstructure transition gradients in titanium dissimilar alloy (Ti-5Al-5V-5Mo-3Cr/Ti-6Al-4V) tailored wire-arc additively manufactured components

J.R. Kennedy, A.E. Davis, A.E. Caballero, M. White, J. Fellowes, E.J. Pickering, P.B. Prangnell

Please cite this article as: J.R. Kennedy, A.E. Davis, A.E. Caballero, et al., Microstructure transition gradients in titanium dissimilar alloy (Ti-5Al-5V-5Mo-3Cr/Ti-6Al-4V) tailored wire-arc additively manufactured components, *Materials Characterization* (2021), https://doi.org/10.1016/j.matchar.2021.111577

This is a PDF file of an article that has undergone enhancements after acceptance, such as the addition of a cover page and metadata, and formatting for readability, but it is not yet the definitive version of record. This version will undergo additional copyediting, typesetting and review before it is published in its final form, but we are providing this version to give early visibility of the article. Please note that, during the production process, errors may be discovered which could affect the content, and all legal disclaimers that apply to the journal pertain.

© 2021 Published by Elsevier Inc.

Microstructure Transition Gradients in Titanium Dissimilar Alloy (Ti-5Al-5V-5Mo-3Cr / Ti-6Al-4V) Tailored Wire-Arc Additively Manufactured Components

J. R. Kennedy[1,2], A.E Davis[1]*, A.E. Caballero[3], M. White[1], J. Fellowes[4], E.J. Pickering[1,5], P.B. Prangnell[1]

[1]University of Manchester, Department of Materials, Manchester, United Kingdom, M13 9PL
[2]Now at Institut Jean Lamour, Campus Artem, 2 allée André Guinier, 54011, Nancy, France
[3]Welding Engineering and Laser Processing Centre, Cranfield University, Bedfordshire, United Kingdom, MK43 0PL
[4]University of Manchester, School of Earth and Environmental Sciences, University of Manchester, M13 9PL, UK
[5]Henry Royce Institute, Manchester, United Kingdom, M13 9PL

(*Corresponding author: alec.davis@manchester.ac.uk)

Keywords: additive manufacturing, titanium, phase transformation, microstructure evolution, EBSD, dissimilar alloy welds

Abstract

The nature of the chemical mixing and microstructure gradients that occur across the interface transition, when manufacturing tailored components with the two high-performance dissimilar titanium alloys (Ti-6Al-4V (Ti-64) and Ti-5Al-5V-5Mo-3Cr (Ti-5553)) by the wire-arc additive manufacturing process, are reported. It has been shown that a relatively long-range chemical gradient occurs during the transition between layers produced with the two different titanium alloys, due to convective mixing in the melt pool between the substrate layers and new alloy wire. This resulted in a stepwise exponential decay composition profile normal to the layers, the width of which can be described by a simple dilution law, with steep local composition gradients seen within the boundary layers at the fusion boundary of each individual layer. The alloy-alloy composition gradients had little effect on the β-grain structure. However, they strongly influenced the transformation microstructure, due to their effect on the parent β-phase stability and the β → α transformation kinetics and reaction sequence. The microstructure gradient seen on transitioning from Ti-64 → Ti-5553 was significantly more abrupt, compared to when depositing the two alloys in the reverse order. Under WAAM thermal conditions, Ti-64 appears to be more sensitive to the effect of adding β-stabilising elements than when Ti-5553 is diluted by Ti-64, because at high cooling rates, stabilisation of the β phase readily suppresses α nucleation when cooling through the β transus, and the normal Ti-64 lamellar transformation microstructure is abruptly replaced by finer scale α laths generated by precipitation during subsequent reheating cycles.

1. Introduction

Additive manufacturing (AM) [1] is becoming an increasingly attractive option for the low-volume production of titanium components in the aerospace sector [2], due to the greater design flexibility and shorter lead times it offers, as well as the greater efficiency of material utilisation made possible by its near-net-shape capability. Of the many AM technologies currently being investigated, wire-arc additive manufacturing (WAAM) – by which parts are built using a wire fed into a translated melt pool formed by a plasma arc [3] – is particularly suited to the production of large-scale titanium components because of its high deposition rate, low cost, and unrestricted build envelope [4]. In addition, by exploiting layer-by-layer fabrication, AM processes can be readily adapted to produce titanium components that have tailored microstructures and graded compositions [5]–[12]. This can include: i) simply varying aspects of the microstructure with a single alloy (e.g. the β-grain size and α inter-lamellar spacing) by managing the thermal conditions [12]; or ii) grading the alloy composition within a component by using two or more feed sources [6]–[11]; or iii) alternating the alloy for each melt track to produce 'alloy-alloy composites' (AACs) [5]. For example, the WAAM process has been previously utilised [5] to deposit an AAC that combined alternating tracks of commercially pure titanium (CP-Ti) with Ti-6Al-4V (Ti-64), to produce the first 'metal composite' example of this technique. However, in this work, it was shown that because mixing occurred in the melt pool, where the new wire was alloyed with the remelted previous layer, distinct tracks of intermediate alternating composition were produced comprised of enriched CP-Ti alloyed with V and Al, and diluted Ti-64 alloyed with CP-Ti.

Although AACs and graded materials can have interesting fracture properties [5]–[11], the composition gradients formed between dissimilar titanium alloy tracks produced by chemical mixing can affect the grain structure and will also create gradients in the α transformation microstructure [8]. The sharpness of such transitions would be expected to have a significant impact on mechanical performance [5], [8], [13]. To produce more efficient titanium components, it is therefore of interest to extend this work further to improve understanding of some of the fundamental challenges involved in using AM processes to achieve tailored, or site specific, properties. Combining Ti-64 with a much stronger material, like the near-β alloy Ti-5Al-5V-5Mo-3Cr (Ti-5553) [14], [15], provides an ideal pair of alloys for studying such an approach, as this combination will potentially allow site-specific properties ranging from very high strength to high damage tolerance. To date, little research has been conducted on the transition between these two materials when deposited by a melt-pool AM process.

Currently, the majority of titanium AM process development has focused on the α + β alloy Ti-64, as it is the most commonly used titanium-based material in aerospace. More recently, other β-stabilised alloys have been investigated [15]–[19], including Ti-5553, Ti-10V-2Fe-3Al, and Beta-C because of their attractive specific properties. The higher strength of β-stabilised alloys, like Ti-5553, arises from the controlled decomposition of the metastable β phase, through solution and ageing treatments, to produce a uniform distribution of fine α-phase precipitates. However, due to the greater concentration of β-stabilising elements (e.g. V, Mo, Cr), and in particular, slow diffusing elements like molybdenum, diffusional phase transformation kinetics in Ti-5553 are much slower than in Ti-64 [14], [20], [21]. In addition, metastable-β solid solutions can potentially decompose by multiple transformation pathways that are highly dependent on the cooling rate and subsequent thermal conditions (e.g. heating rate) [14], [19]–[21]. In the as-deposited state, a greater level of micro-segregation is also expected within the parent β grains in this alloy than in Ti-64, due to the greater deviation of the partition coefficients of the main alloying elements Mo and Cr from unity [22]–[24]. As a result, the AM microstructures of as-deposited β-stabilised alloys and Ti-5553 can be considerably different to those found for Ti-64, and are highly dependent on the cyclic thermal conditions experienced during a particular AM process [14], [15], [20], [25].

Of particular interest to the mechanical performance of a dissimilar alloy AM component is the alloy-alloy transition composition gradients that will occur by definition within the material and the effect this

will have, when combined with the unique cyclic thermal history in an AM process, on the final microstructure. During AM, the deposited material is reheated multiple times by the passage of the heat source, with much faster heating and cooling rates (~500°C and ~30°C s^{-1}, respectively in WAAM [26]) than seen in conventional heat treatments. When depositing Ti-64 in the WAAM process, the last ~5 added layers are typically reheated above the β transus temperature (~980°C [26], [27]) and transform to α during cooling, so each added layer in Ti-64 experiences several β → α → β phase transformations [26]. In comparison, Ti-5553 has a lower β-transus temperature (~850°C [14], [25], [28]) and the β phase is stable enough to prevent diffusional transformation during cooling at these high rates [15], [19], [29], although athermal reactions can occur (e.g. ω phase [14], [30], [31]). In addition, with Ti64, there is a temperature interval below the β transus where rapid coarsening of the transformed α can occur as the β fraction increases on reheating, which is in the range of the β approach curve. This leads to the appearance of HAZ bands that appear in the microstructure as a locus of the peak temperature rise in the range ~750 – 1000°C within the thermal field generated by the moving heat source [26]. However, with Ti-64 when subsequent layers are added, little further microstructural change occurs as the peak temperatures experienced by the material drops below 700°C [26]. In comparison, in Ti-5553, because the metastable β phase is stable at lower cooling rates than experienced in AM processes [32], α forms by precipitation during reheating rather than on cooling [14], [30]–[32]. This results in a microstructure transition between the fully-β top part of a build and the onset of heterogeneous α precipitation, before the 'steady-state' region of the deposit is reached where no more precipitation occurs, as the peak temperature rise becomes too low to have any further influence [15], [19], [29]. Given the multiple heating cycles that occur in AM processes, and the steep local temperature gradients experienced by the material under the translated heat source, it is encouraging that in Ti-5553 these heterogeneous thermal conditions are still reported to result in a relatively uniform density of α precipitates, similar to that seen in a conventional 'overaged' microstructure [33].

To improve current understanding of the constraints imposed by producing large dissimilar alloy-alloy tailored components with high deposition rate processes like WAAM, the main aim of the work presented here was thus to investigate the extent and distribution of chemical mixing that occurs across dissimilar Ti-5553 ↔ Ti-64 alloy transitions, when co-depositing these two materials, and to determine the impact this can have on the microstructure gradients created, once steady state is achieved; i.e. when sufficient layers have been added such that no more thermal effects are experienced. This knowledge can then be used to help design future, more-complex tailored components using this, or similar alloy combinations. Since, in WAAM, chemical mixing with the previously deposited material is substantial [34], [35], and the effect of the β-phase stability on the transformation microstructure is known to be important and sensitive to the thermal history, two Ti-5553/Ti-64 transitions were created: one where layers of Ti-64 were deposited first before adding Ti-5553, and one where the order of addition was reversed. The chemical mixing across the alloy transition was investigated using electron probe microanalysis (EPMA) and energy dispersive X-ray spectroscopy (EDS), and the microstructure and macro-variation in α inter-lamellar spacing was investigated using a combination of high resolution scanning electron microscope (SEM) backscatter electron (BSE) imaging and electron backscatter diffraction (EBSD). The complex material behaviour observed is discussed as a function of the molybdenum-equivalent β-phase stability and the response of the local compositions to the rapid thermal cycles experienced in the WAAM process.

2. Experimental Methods

To investigate Ti-5553 ↔ Ti-64 alloy layer transitions with the WAAM process, model samples were built using two feed wires, comprised of multiple layered sections of Ti-5553 and Ti-64. A cross-wall oscillation path build strategy was implemented [36], [37] with a 12 mm width, to build samples representative of typical wide section parts (see Fig. 1). The Ti-64 wire was deposited first to a build

height of 40 mm, after which the wire feed was changed to Ti-5553 and a further 65 mm was deposited, and finally the wire was changed back to Ti-64 before the top 40 mm was deposited. This sample design was employed to allow characterisation of a transition from both Ti-64 → Ti-5553 and the reverse sequence of Ti-5553 →Ti-64, with sufficient layers added with each material to ensure steady state conditions were reached in each transition. Deposition was carried out using the standard WAAM parameters provided in Table 1, and the reference frame layer normal direction (ND) wall length (WD) and transverse directions (TD) and sample dimensions are defined in Fig. 1. After deposition, the samples were removed from the substrate and ND-TD cross sections were cut from the centre of the wall for metallographic characterisation.

Table 1. WAAM deposition parameters.

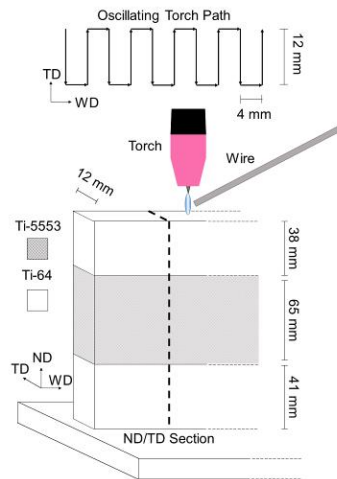| WAAM build parameters	
Travel Speed	5 (mm s^{-1})
Current	170 (A)
Wire Diameter	1.2 (mm)
Layer Height	~1.5 (mm)
Plasma Gas Flow	0.013 (L s^{-1})
Wire Feed Speed	2 (m min^{-1})

Figure 1. Test sample schematic showing the oscillating heat source path, reference frame, and location of cross sections taken for metallographic investigation. The sample reference directions are defined as: WD ≡ heat source travel, or 'welding' direction, TD ≡ transverse direction, and ND ≡ build height, or 'normal' direction.

Samples were prepared for metallographic examination using silicon carbide grinding papers and subsequently polished with a 0.25 µm colloidal silica suspension (OPS), containing 5% hydrogen peroxide. After etching samples with Kroll's Reagent, optical microscopy was performed with a Zeiss Axio Imager 2, with automated stage scanning to produce large-area high-resolution stitched images. SEM-BSE imaging was conducted on an FEI Magellan FEG-SEM, using an accelerating voltage and probe current of 5 kV and 0.4 nA, respectively, and micrograph tile 'line scans' were acquired for automated image analysis using the FEI MAPS image stitching software. Through this approach, 300 – 400 by 3 wide image tile strips with a width of 15 µm were acquired, automatically and at high resolution, so the α inter-lamellar spacing in the Ti-64, the α lath dimensions in the Ti-5553, and the mixed α + β microstructures in the alloy transitions could be quantified using an in-house batch processing image analysis routine. For this analysis, micrographs were pre-processed by first applying

a homomorphic high-pass Gaussian filter to normalise image intensity [38]. The optimal threshold for image segmentation was then selected via Otsu's method [39], which iteratively searches the normalised image intensity histogram for the threshold which maximises the between-class variance. Each image was then binarised according to its optimal threshold, such that pixels containing the α phase are assigned a value of 1 and the β phase a value of 0. Finally, area closing [40] was used conservatively to remove the fine-scale mislabelled β matrix from the α laths. A Python script was written following ASTM 1382-97 [41] to determine the average inter-lamellar spacing. 200 random line scans were performed on each frame and a histogram of chord lengths intersecting α laths was constructed. This enabled the variance to be quantified. The β-phase fraction was quantified simply as the ratio of black to white pixels in the binarised images. The Python script used is available on GitHub [42].

EBSD and EDS mapping was carried out simultaneously on an ultra-high speed EBSD platform comprised of a Thermo Fisher Apreo C FEG-SEM, integrated with an Oxford Instruments' Symmetry 2 EBSD detector, AZtec acquisition software, and an Ultim Max EDS detector. EBSD mapping was performed using an accelerating voltage of 20 kV, and large low-resolution and smaller high-resolution maps were acquired using probe currents of 51 and 1.6 nA, a stage tilt of 70 and 75°, and a step size of 20 and 0.1 μm, with data collected at 3000 and 45 Hz, respectively. EBSD maps were processed with Oxford Instruments' AZtec Crystal software and are displayed in inverse pole figure (IPF) colouring relative to the build-height direction (ND). β-phase EBSD maps of Ti-64 were reconstructed from the collected α phase data using software developed by Davies and Wynne [43], [44] where a 2° misorientation maximum from a particular α variant was accepted, and up to a 3° divergence from the BOR was considered part of the same parent β grain. All textures are depicted in contoured pole figures and scaled in multiples of random density (MRD). For the EDS maps, only results for Al and Mo are presented, since the X-ray peak overlaps of Ti, V, and Cr could not be reliably resolved in the EDS spectra. Higher chemical sensitivity analysis was achieved by using a JEOL JXA-8530F FEG-EPMA equipped with 4 wave-dispersive spectrometers (WDS), enabling all the elements of interest to be quantified. The EPMA line scans were acquired using an accelerating voltage of 15 kV, a current of 100 nA, and a step size of ~70 μm; and counts for Al ($K_{\alpha1}$) were collected on a TAP diffraction crystal, Mo ($L_{\alpha1}$) on a PET crystal, and Fe ($K_{\alpha1}$), Cr ($K_{\alpha1}$), and V ($K_{\alpha1}$) on a LiFL crystal.

3. Results

3.1. Alloy-Alloy Transition Overviews and Bulk Textures

Optical images showing overviews of the Ti-64 ↔ Ti-5553 alloy-alloy transitions sectioned in the normal-transverse plane (ND-TD) are provided in Fig. 2. The regions with α precipitation in the Ti-5553 alloy etch more aggressively and appear dark in the macrographs [15]. At this magnification, from the etching contrast, relatively sharp and curved fusion boundaries can be seen between the two materials for the Ti-64 → Ti-5553 transition, when the first layer was deposited with the new alloy (Fig. 2a), whereas a more step-like gradation in the etching contrast can be seen for the Ti-5553 → Ti-64 transition (Fig. 2b). The etching profiles of the layer bands are consistent with that expected for the fusion boundary in the WAAM process [26], [45]. HAZ bands can also be seen in the Ti-64 deposited material, appearing as near-horizontal lines of dark-to-light contrast, which are equally similar to those found in monolithic Ti-64 samples built with the same oscillation strategy (e.g. [26], [36], [46]–[50]). In comparison, no HAZ bands can be seen in the Ti-5553 material, but instead narrow curved bands of lighter contrast can be observed following each fusion boundary. The origin of this second type of banding has been previously discussed in ref. [26] and is caused by transient solute partitioning, which takes place when the solidification velocity first accelerates from the fusion boundary. These fusion boundary 'transient segregation' bands are much more pronounced in the Ti-5553 than the Ti-64 alloy, due to the greater deviation of the partition coefficients (k) from unity of Mo and Cr, compared to Al and V. During solidification, Mo and Cr in the Ti-5553 alloy also micro-segregate in inverse directions, with Mo, $k = 2$ [22], [24], concentrating in the dendrite cores, and Cr, $k = 0.81$ [23], in the interdendritic

regions. Due to the shorter etching time employed because of the greater reactivity of the α precipitated regions in the Ti-5553 alloy, the weaker transition segregation bands are not as visible in the Ti-64 layers, where in prior work they have been attributed to Fe segregation [26]. The presence of β-grain boundaries (GBs) and evidence of a very coarse columnar β-grain structure can also be seen in the optical images for both transition regions (Fig. 2).
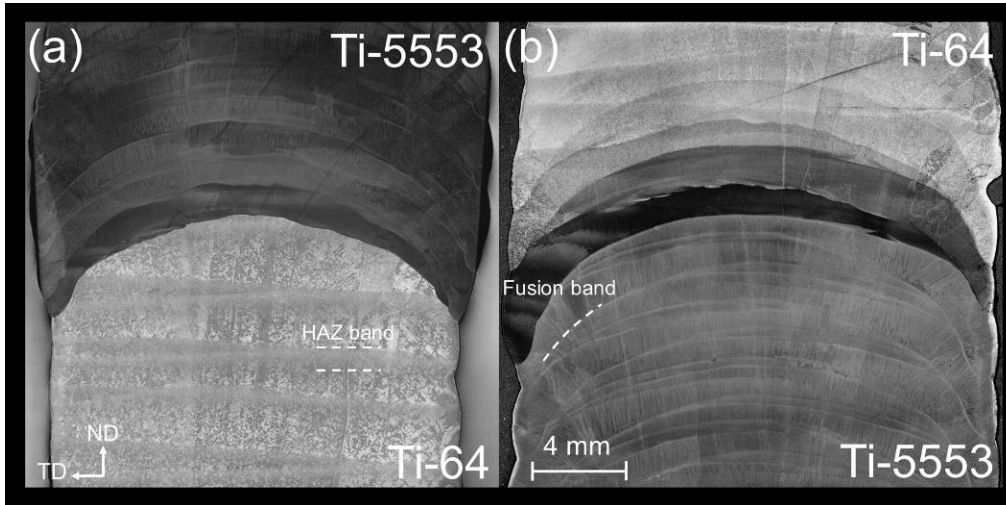

Figure 2. Optical macrographs from etched samples, showing the transition regions between the two alloys when deposited in alternate order: (a) for Ti-64 → Ti-5553 and (b) Ti-5553 → Ti-64. The images are from normal-transverse (ND-TD) cross sections.
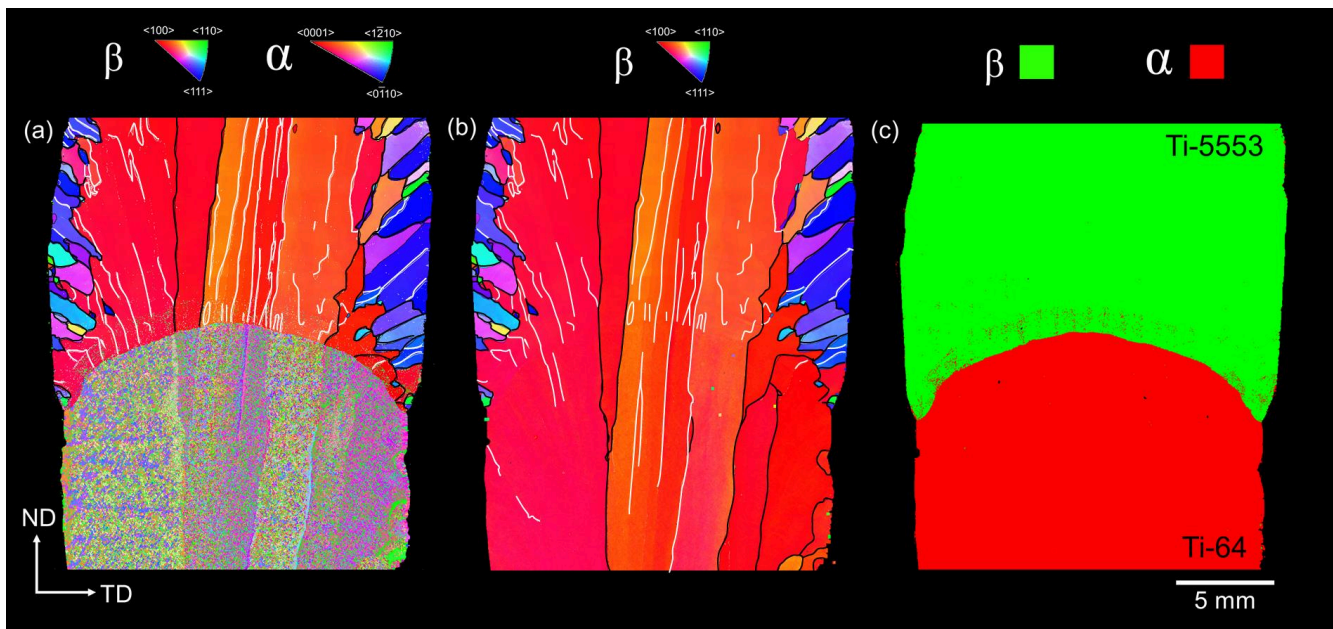

Figure 3. Macro-scale large area EBSD ND-TD maps from the Ti-64 → Ti-5553 transition sample, showing: (a) an orientation map of both α and β phases in inverse pole figure colouring with reference to the build-height direction (ND), (b) the β-phase grain structure (recombined using reconstruction for the undiluted Ti-64 base region) and (c) a phase indexing colour map. Low angle (> 5°, < 15°) grain boundaries and high angle (> 15°) grain boundaries are highlighted as white and black lines, respectively, in (a) and (b).

In Fig. 3, large area EBSD maps are provided across the Ti-64 → Ti-5553 alloy-alloy transition in Fig. 2a, showing: (a) the texture of the α and β phases, (b) the β-phase grain structure only, and in (c) an α + β phase map. It should be noted that in Fig. 3b, due to the low residual β volume fraction in the Ti-64 base layers, the β-phase orientations had to be reconstructed from the indexed α phase data and this was merged with that for the Ti-5553 region where the β phase could be directly indexed. As expected, the phase map (Fig. 3c) shows that the un-diluted Ti-64 bottom section is dominated by the α phase and the Ti-5553 top layers by β. However, it should be noted that, at this coarse scale, the α + β microstructure detail in the transition region is missed due to the large EBSD step size employed and, as indexing of the fine α precipitated in the Ti-5553 and the residual β in the Ti-64 rich regions is very poor, the phase map is artificially dominated by the matrix β and the transformed α, above and below the alloy-alloy transition, respectively.

In Fig. 3b, it can be further seen that the large columnar β grains present exhibit strong $\langle 001 \rangle_\beta$ alignment with the build-height direction (ND) and most of their boundaries are relatively 'low angle', being less than < 15° in misorientation (highlighted white). If a conventional 15° misorientation threshold is used to distinguish high angle grain boundaries (HAGBs: highlighted black in Fig. 3b), this strong texture therefore means that the effective 'grain size' is very large, with the columnar gains being ~ 2 – 5 mm wide. For example, the top (Ti-5553) part of the wall only contains 3 'grains' across its entire width, mutually misorientated by > 15°. In addition, the Ti-5553 alloy has developed an exterior casing of finer more randomly orientated grains that have grown aligned towards the wall surfaces, which are not seen in the Ti-64 lower section of the sample. Although, after deposition, the lower Ti-64 section was dominated by the α phase, in Fig. 3a the α micro-texture variation, and the presence of single-variant grain boundary α colonies in the EBSD data, highlights the parent β-grain boundaries [36], [51] and confirms that the β-grain structure has been accurately reconstructed in the merged map shown in Fig. 3b. From this composite β orientation map, it is apparent that the columnar β grains (both low and highly misorientated) have grown epitaxially from the fusion boundary in each pass [46], [52], [53] and continued uninterrupted through the alloy-alloy transition region, despite the changes in melt-pool composition, to go on to span the entire height of the sample area.
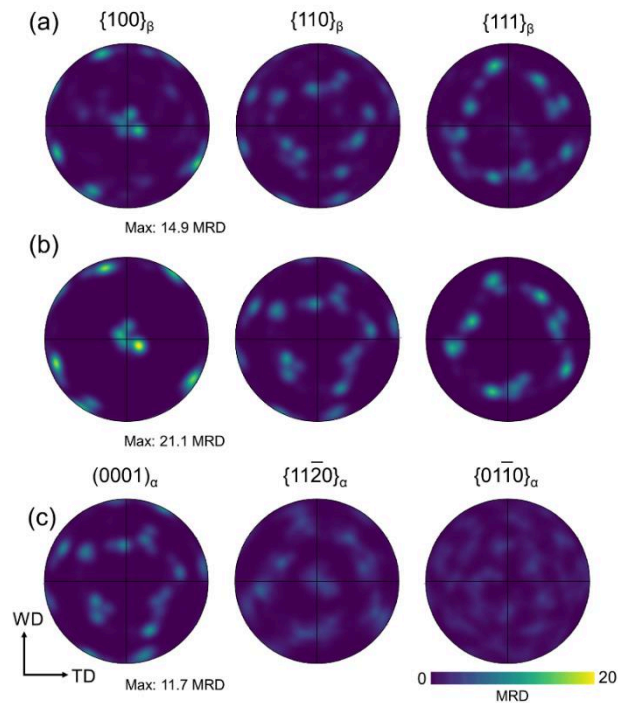
Figure 4. Pole figures depicting the textures from the EBSD maps shown in Fig. 3: (a) the top Ti-5553 section β phase, (b) the reconstructed β phase of the base Ti-64 layers, and (c) the as-indexed α phase of the base Ti-64 layers.

Pole figures obtained from the maps in Fig. 3 are shown in Fig. 4, where it can be seen that the texture from the lower section Ti-64 layers in the reconstructed β phase pole figures (Fig. 4b) closely matches that of the directly indexed β phase in the upper section of the Ti-5553 alloy (Fig. 4a), consistent with the columnar β grains growing continuously from the Ti-64 base section into the Ti-5553 rich layers. Although the texture data was collected from a limited number of columnar β grains, overall, the β-phase pole figures (Fig. 4a and b) show strong $\langle 001 \rangle_\beta$ || ND alignment, which is common in titanium alloys with columnar grain structures produced by DED-AM [15], [53], [54]. For the top Ti-5553 region, the weaker non-$\langle 001 \rangle_\beta$ || ND orientations in the $\{100\}_\beta$ pole figure originate from the finer surface grains seen in Fig. 3a. These orientations appear with lower strength in the pole figures because they contribute a relatively small area to the EBSD map, but still dilute the intensity of the dominant $\langle 001 \rangle_\beta$ || ND component relative to that seen for the Ti-64 section of the wall (Fig. 4b). In addition, since the Ti-64 base layers contain a highly textured columnar β-grain structure, the α-phase transformation texture (Fig. 4c) from this region is also relatively strong, with a maximum of 11.7 MRD, which is again comparable to that found in a typical Ti-64 monolithic WAAM deposit [53], [55].

3.2 Composition Gradients

To investigate the chemical gradients formed when producing the alloy-alloy transitions, relatively coarse step size (~70 μm) electron probe micro-analysis (EPMA) line scans were performed normal to the layers (i.e. in ND). From Fig. 5, it is immediately apparent that long-range chemical mixing occurred during deposition of the WAAM samples. The overall chemical transition between the two alloys spanned up to ~4 mm for both build sequences and varied in a 'stepwise' exponential profile, comprised of near-constant composition 'ledges' across each added layer, with abrupt steep gradients near the fusion boundaries between individual layers. The nominal composition of the second alloys were also not approached until at least the third layer was deposited with the new wire, and trace amounts (≤ 0.2 wt.%) of residual alloy elements were still found to be carried forwards into the fourth and fifth layers with the new alloy (e.g. Mo and Cr when Ti-64 was deposited on Ti-5553; Fig. 5b). This long range, step-wise, exponential decay in the average composition of each new added layer is consistent with the alloy-alloy composition transition profiles being dominated by melt-pool dilution, and resulted in the greatest change in composition occurring when the first layer was added with the alternative wire. It can also be noted, that in the EPMA measurements, the composition within each individual layer was not always uniform, suggesting full melt-pool mixing had not always occurred, as can be seen most clearly from the local variation in the Mo and Cr concentrations across layers 1 & 2 in Fig. 5a.

The average compositions measured for the base alloys and each added layer (averaged over the composition steps) across the transition regions obtained from the EPMA data are summarised in Table 2, along with their 'molybdenum equivalence' index (Mo_{eq}) [14]. This empirical measure of β-phase stability can be seen to increase sharply by a factor of Mo_{eq} = 7 when the Ti-5553 alloy was first deposited on Ti-64, but changed less severely by Mo_{eq} = 4.9 in the first new layer when the alloys were deposited in the opposite order. Depositing Ti-5553 on Ti-64 thus created a more rapid change in the β-phase stability index than with the reverse order.
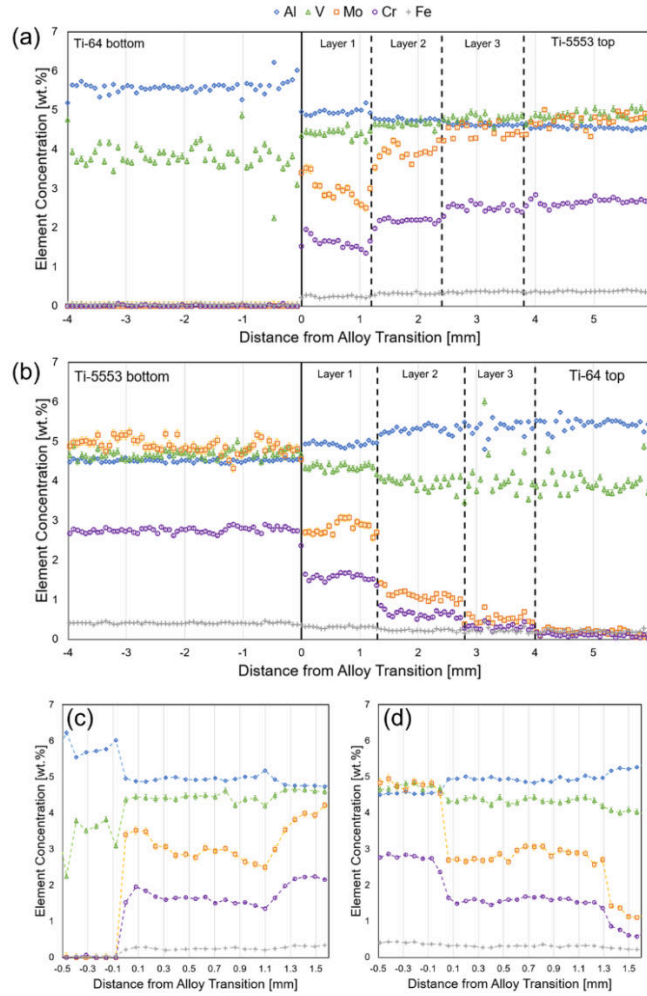
Figure 5. Electron probe micro-analysis line scan composition profiles across the interfaces of (a) Ti-64→Ti-5553 and (b) Ti-5553→Ti-64. (c) and (d) show the respective first new layers at a higher magnification.

Table 2. Average layer compositions measured from the EPMA data for the WAAM sample base alloys and 4 layers after deposition of the new alloy. The β-phase fraction ($β_f$) measured by backscatter electron image analysis is also provided, as well as the molybdenum equivalence (Mo_{eq}) determined from the compositions [14].

Sample	Layer	Al [wt.%]	V [wt.%]	Mo [wt.%]	Cr [wt.%]	Fe [wt.%]	βf [%]	Mo_{eq}
Ti-64 bottom	0	5.51	3.81	0.00	0.01	0.04	10.9	-2.8
	1	4.93	4.39	2.96	1.61	0.24	34.2	4.2
	2	4.74	4.64	3.92	2.17	0.32	40.4	6.7
	3	4.63	4.79	4.48	2.53	0.37	43.6	8.2
	4	4.57	4.82	4.64	2.60	0.37	47.1	8.5
Ti-5553 top		4.52	4.94	4.86	2.70	0.38		9.1
Ti-5553 bottom		4.52	4.72	4.88	2.75	0.40	49.7	9.1
	1	4.93	4.34	2.82	1.57	0.31	34.7	4.2
	2	5.30	3.96	1.12	0.65	0.23	19.6	0.2
	3	5.34	4.08	0.53	0.32	0.22	13.7	-0.9
	4	5.45	3.95	0.20	0.11	0.20		-1.8
Ti-64 top		5.48	3.92	0.10	0.06	0.18		-2.1

3.3 Microstructure Transition Gradients

Higher resolution investigation by SEM, EDS, and EBSD revealed complex transitions had occurred in the transformation microstructure within the composition gradients between the two alloys, which depended on the order of deposition (i.e. Ti-64 → Ti-5553, or Ti-5553 → Ti-64). Backscatter electron (BSE) micrographs of the microstructure found within each (layer) composition step (Fig. 5), after Ti-5553 was deposited on Ti-64, are shown in Fig. 6. The steep local microstructure gradient seen across the fusion boundaries between the undiluted Ti-64 sample base and the first layer, and the first and second layers, added with the new Ti-5553 wire are also shown at higher magnification in Fig. 7.

The transformation microstructure in the undiluted Ti-64 base layers, before Ti-5553 was deposited, can be seen in Fig. 6a and is characteristic of a normal monolithic WAAM Ti-64 sample manufactured with the oscillation build strategy, which produces slower cooling rates than in a single-pass-wide wall [36]. It consists of a relatively coarse lamellar α microstructure (inter-lamellar spacing ~1 μm) with a 'basketweave' morphology, formed by packets of interpenetrating single-variant α laths, and contains thin ~100 nm residual films of ~10% retained β. From Fig. 6, it can be seen that the α transformation microstructure becomes substantially finer through the next 3 subsequently added layers (Fig. 6b → f) as the Ti-64 alloy becomes progressively enriched with the Ti-5553 wire, which increases the concentration of β-stabilising elements (Table 2, Fig. 5a). However, the most dramatic change occurred across the fusion boundary in the first layer deposited with the Ti-5553 wire (Fig. 6a → b); and by the third layer (Fig. 6f), the α lath size and morphology is comparable to that seen for α precipitation in a monolithic Ti-5553 AM build [15].
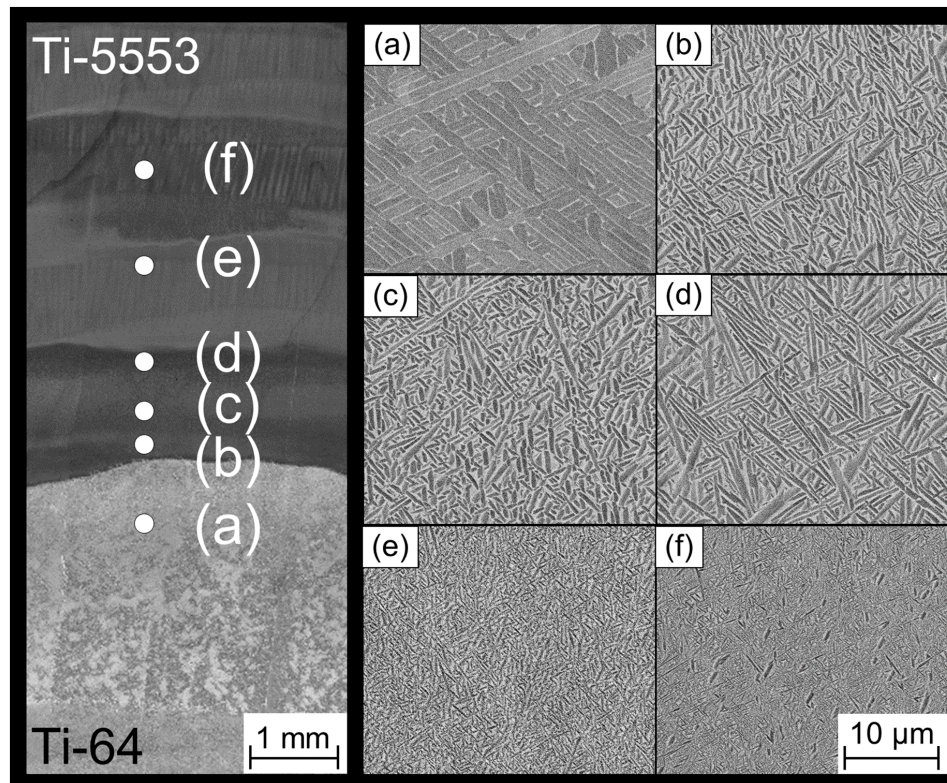

Figure 6. SEM backscatter electron micrographs showing representative changes in microstructure across the first 3 new added layers of Ti-64 to Ti-5553 transition, with their location shown on the corresponding optical macrograph.

The microstructure gradients seen across the fusion boundaries after the first Ti-5553 layer was added, and between the first and second layers, are shown at higher resolution in Fig. 7a and b. An abrupt α-lath scale and morphological transition clearly occurs within the compositional boundary layer formed at the base of the first new Ti-5553 rich melt track, which resulted in a sudden reduction in the α lath size. When the first Ti-5553 layer was added, the α laths reduced in width and aspect ratio from ~1 to ~0.4 μm and > 20:1 to 5:1, over a relatively short distance of ~50 μm. In comparison, the next fusion boundary microstructure gradient was less severe when the second Ti-5553 layer was added and resulted in a further reduction in lath size to ~ 0.3 μm in width (Fig. 6-7). Fig. 7a also shows that the area fraction of β phase (lighter contrast) increased over a relatively short distance from the fusion boundary, as the Ti-64 base composition was diluted and enriched with a greater concentration of β-stabilising elements in the first Ti-5553 added layer.

Moving up from the first fusion boundary produced with the Ti-5553 alloy, the coarse α laths seen in the Ti-64 base layer appear to first develop more branches – dividing repeatedly into finer multiple parallel α lamellae (Fig. 7c) before suddenly evolving into a bimodal distribution comprised of longer α laths, embedded in a matrix of apparently much smaller, lower aspect ratio laths that contains a larger fraction of retained β (Fig. 7d). Finally, the remaining larger high aspect ratio laths disappear to be replaced completely by the much finer, low-aspect-ratio, α laths and the overall size distribution becomes more homogeneous. As the dilution of Ti-64 by Ti-5553 increases, this same finer α microstructure is then seen to continue across all of the subsequent layers and there is a progressively smaller, but still noticeable, reduction in the scale of the α laths across each subsequent fusion boundary with the second and third Ti-5333 added layers (Fig. 7b).

The variant orientations seen across the first severe microstructure gradient from the fusion boundary – when the Ti-5553 alloy was initially added – are shown in the high resolution EBSD maps in Fig. 8; where Fig. 8a-e depicts ~0.7 mm above the fusion boundary (white dotted line), which is over half the layer thickness (~1.2 mm), and Fig. 8f and g provide magnified views across the first ~100 μm that contains the initial steep composition gradient. In the lower magnification phase map in Fig. 8a, the area fraction of β indexing can be seen to rapidly increase with distance in ND. However, there are also two bands of higher β volume fraction above the fusion boundary that correspond to more concentrated regions of molybdenum in the EDS map in Fig. 8e. This provides additional evidence of the local effect of incomplete mixing near the base of the melt pool, after which, with greater build height, the solute distribution and phase fractions are seen to become more uniform. The β-phase orientation data in Fig. 8b demonstrates that the map region in Fig. 8 consisted of a single β orientation, which was part of one of the large columnar grains seen in Fig. 3b. Within this single parent β orientation, the areas of locally higher β-phase fraction seen in Fig. 8a correspond to regions of significant α orientation variant selection – shown in the α-phase orientation map in Fig. 8c – where in region (i) there are dominant $\langle 0\bar{1}11 \rangle_\alpha \parallel$ ND variants (purple, 2/12 of possible BOR orientations) and (iii) is dominated by $\langle 0\bar{1}10 \rangle_\alpha$, $\langle 11\bar{2}0 \rangle_\alpha$, and $[0001]_\alpha \parallel$ ND variants (blue, green, and red, respectively; 6/12 of possible variants). However, farther away from the interface, where the α laths are much finer, the α variants become more randomly distributed.

The additional higher magnification EBSD maps in Fig. 8f and g provide orientation data that can be correlated to the rapid α morphological transition seen in the SEM images in Fig.7. Immediately below the fusion boundary of the first Ti-5553 layer, in the undiluted Ti-64, the transformation microstructure is considerably coarser and can be seen to contain larger single-variant α colonies, comprised of high-aspect-ratio laths. (It should be noted that these colonies contain parallel α lamellae with the same orientation, so that the individual lath boundaries are not discernible in the EBSD map). On transformation during cooling below the β transus, some of the larger α laths that formed these colonies (see ref. [56]) have grown further up into where the melt pool became richer in Mo and Cr, to form the very large high-aspect-ratio laths seen in the bimodal α distribution found in the SEM images taken of the microstructure transition seen in Fig. 7d. In the map area studied, these remaining coarse

laths had a single variant orientation ($\langle 11\bar{2}0 \rangle_\alpha$ || ND) and penetrated ~30 µm into the transition region at a 47° angle to ND. However, without more data, it is not known if this is significant and it may just reflect the particular orientation of a specific α colony that formed in the Ti-64 alloy closest to the fusion boundary with the first Ti-5553 layer, within this local map area. Farther up from the fusion boundary, above where these large laths cease, a second distribution of much finer α laths can be seen to have formed, grouped in multi-variant colonies consisting of 3 or more α variants [36] and the microstructure became more uniform. In the bimodal-lath-size transition between these two transformation microstructures, the second distribution of much finer α laths have 'filled-in' the matrix between the coarser high aspect ratio laths that continued to grow out from the coarse single variant colonies that developed in the Ti-64 base layer.
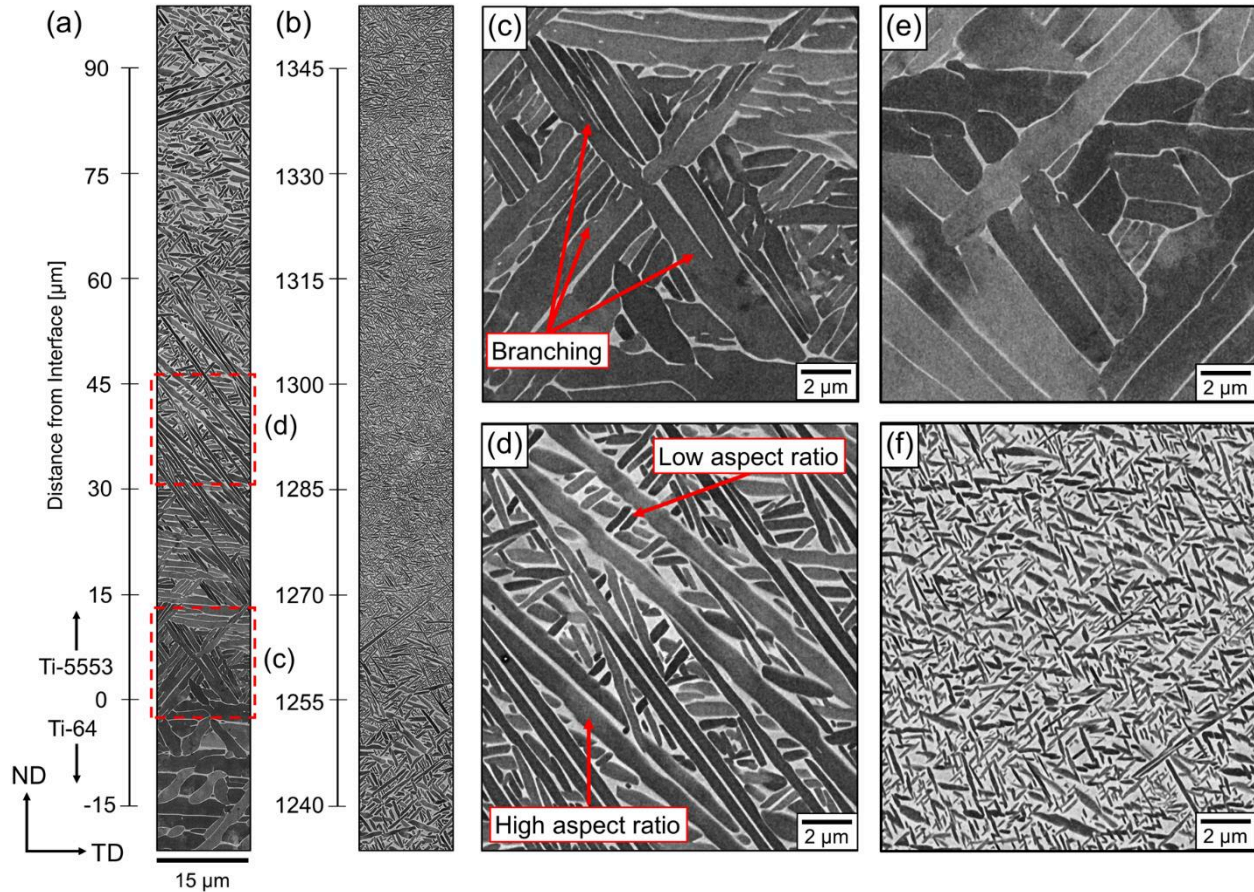

Figure 7. SEM backscatter electron micrographs showing: (a) the initial steep fusion boundary microstructure transition when the first Ti-5553 layer was deposited on Ti-64, and (b) the second microstructure gradient between Ti-5553 layers 1 and 2 (Fig. 6d → e). The y-axis is the distance from the first fusion boundary with the Ti-5553 alloy. (c-d) show the morphological changes at higher magnification across the sharp transition gradient seen at the first fusion boundary (from areas highlighted in (a)). Typical baseline Ti-64 and Ti-5553 microstructures are provided in (e) and (f) for comparison.
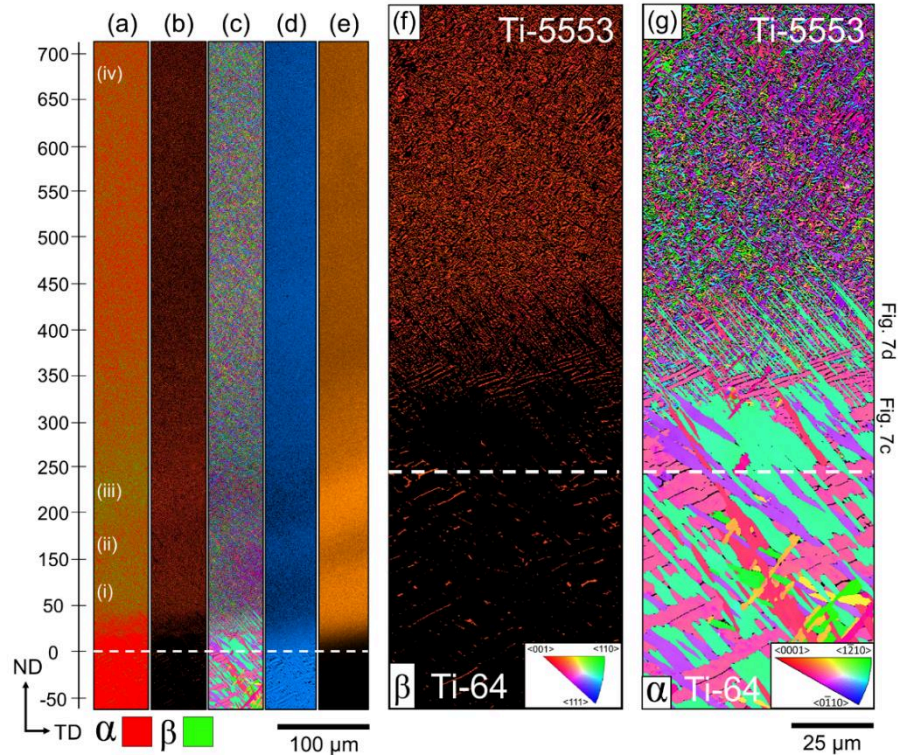
Figure 8. High resolution EBSD maps obtained across the fusion boundary transition from Ti-64 into the first Ti-5553 added layer, with respect to the build-height direction (ND): (a) shows the indexed α and β-phase distributions, (b, f) and (c, g) show β and α phase orientation maps, respectively, in IPF // ND colouring; and (d) and (e) show EDS maps of Al and Mo, respectively. Regions (i-iv) correspond to β-phase fractions of 38.6, 37.4, 38.1, 34.9%, measured by backscatter electron image analysis (see Fig. 12). In (f) and (g), high magnification β and α IPF orientation maps are provided of the abrupt transition seen in the α morphology across the first fusion boundary.

Overall, it can thus be concluded that when layers of Ti-5553 were deposited on Ti-64, the microstructure transition seen in the transformation structure developed in a stepwise fashion and was particularly abrupt at the first fusion boundary formed with the new alloy (Fig. 6). In comparison, a more gradual microstructure transition was found when the alloys were deposited in the opposite order (Ti-5553 → Ti-64). An overview of this 'reversed' transition gradient is shown in Fig. 9 and the first 100 µm above the first fusion boundary with the new alloy is shown at higher magnification in Fig. 10. The typical WAAM microstructure of the undiluted Ti-5553 alloy below the transition is depicted in Fig. 9a and consists of very fine 0.1 µm-thick α laths that have precipitated in small tri-variant colonies [36] with about 50% retained β and an α lath aspect ratio of ~3:1. Across the fusion boundary with the first new layer added with Ti-64 (Fig. 9b & 10d), there is a rapid increase in the α phase fraction (darker contrast) and the β-phase volume fraction dropped to ~30%, but the change in size of the laths was relatively small compared to the more abrupt transition seen before the alloy deposition order was reversed (Fig. 6). The average α lath aspect ratio also only increased from 3:1 to ~5:1 from the Ti-5553 substrate into the first added Ti-64 layer. In contrast to with the Ti-64 → Ti-5553 transition, the higher resolution BSE images of the microstructure gradient in Fig. 10a show this more gradual change in α lath size took place without any major morphological transition. In addition, between the first deposited Ti-64 layer (Fig. 9c-d), and layers 2 (Fig. 9e), and 3 (Fig. 9f), the microstructure evolution became progressively even more gradual and, with reducing concentrations of β-stabilising elements, the α laths simply slowly increased in size across each new layer boundary (Fig. 5b) until they converged with the coarser basketweave Ti-64 parent microstructure after approximately 3 more added layers.
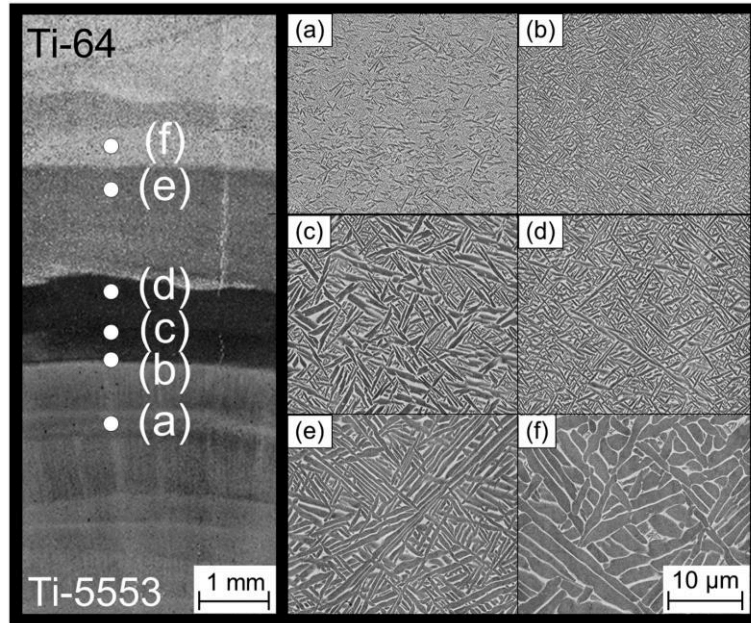
Figure 9. SEM backscatter electron micrographs showing representative images of the microstructure transition from Ti-5553 to Ti-64. Their location is shown on the accompanying optical macrograph.
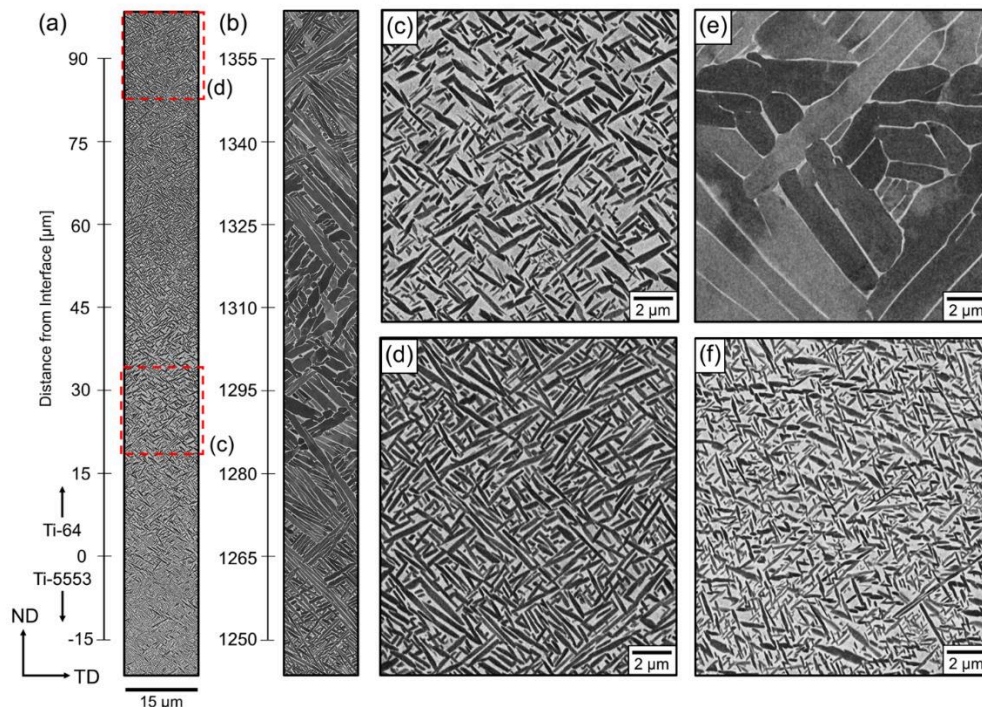

Figure 10. SEM backscatter electron micrographs of the reverse Ti-5553 →Ti64 alloy transition: (a) across the initial fusion boundary, when the first layer Ti-64 was deposited on Ti-5553, and (b) the second microstructure transition between layers 1 and 2 (Fig. 9d → e). The y-axis is the distance from the fusion boundary with the first Ti-64 layer fusion boundary. (c-d) show the different α lath sizes and the change in β-phase fraction during the first fusion boundary transition gradient (areas highlighted in (a)). Ti-5553 and Ti-64 base microstructures are again provide in (e) and (f) for comparison.
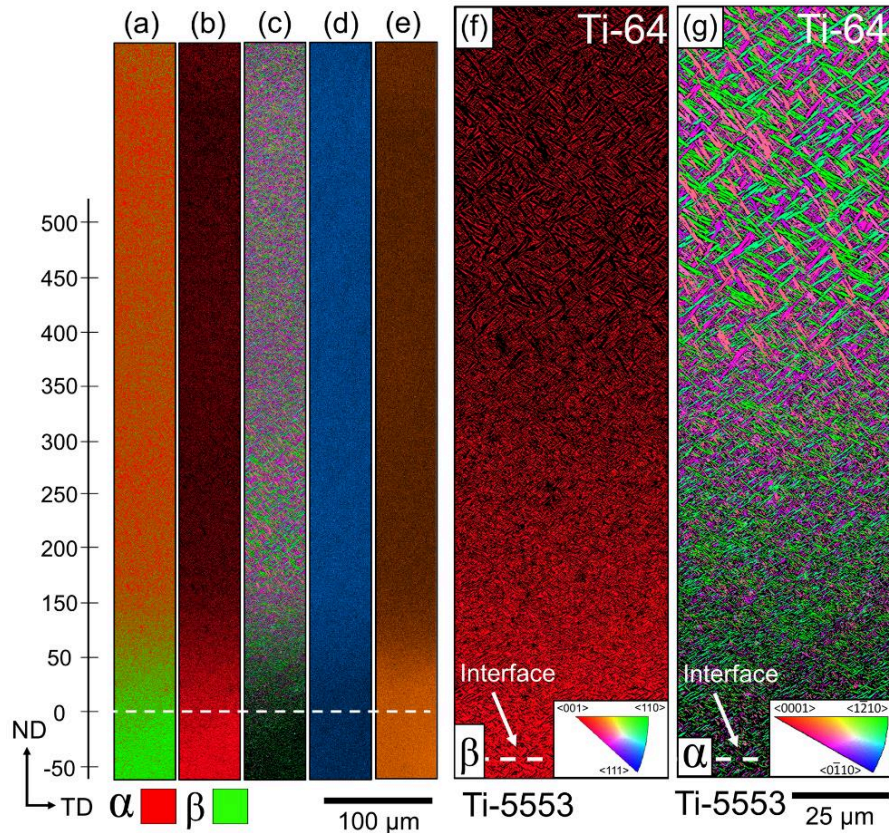
Figure 11. EBSD maps of the transition across the fusion boundary from Ti-5553 into the first Ti-64 added layer, with respect to the build-height (ND): (a) shows the indexed α and β-phase distributions, (b, f) and (c, g) show β and α phase orientation maps, respectively, in IPF // ND colouring; and (d) and (e) show Al and Mo EDS maps. In (f) and (g), high magnification β and α IPF orientation maps are provided of the transition seen in the α phase near the fusion boundary. Note: the very fine scale of the Ti-5553 microstructure seen at the bottom of the map is beyond the limit for reliable EBSD indexing and pattern overlap may cause biasing of the indexed orientations.

To more accurately quantify the microstructure differences across the alloy-alloy layer transitions, the average α lath widths and phase volume fractions were extracted using automated image analysis from high resolution SEM-BSE image maps (as detailed in §2) to create distance profiles. The resultant data sets in Fig. 12 show a stepwise behaviour mimicking the chemical line scans in Fig. 5. Across both transitions, the β-phase fraction varied from ~10% in the Ti64 to 50% in the Ti-5553 base alloys, and the average phase fractions for each layer have been added to Table 2. Similarly, the α lath thickness changed from ~0.1 – 0.9 μm in steps across each layer, with the finest laths occurring in the Ti-5553 microstructure. Therefore, there will be a stepwise gradient in yield strength across each alloy-alloy transition, which would be expected to increase and decrease across the Ti-64 → Ti-5553 and Ti-5553 → Ti-64 transitions, respectively. Additionally, the plots in Fig. 12 again show the influence of incomplete solute mixing within each added layer. This is exemplified in Fig. 12c, where there are two peaks in the β-phase fraction (also identified in the EBSD map in Fig. 8a) that correspond to varying levels of β-stabilising solute elements (Fig. 5), particularly the molybdenum concentration (Fig. 5 and 8e).
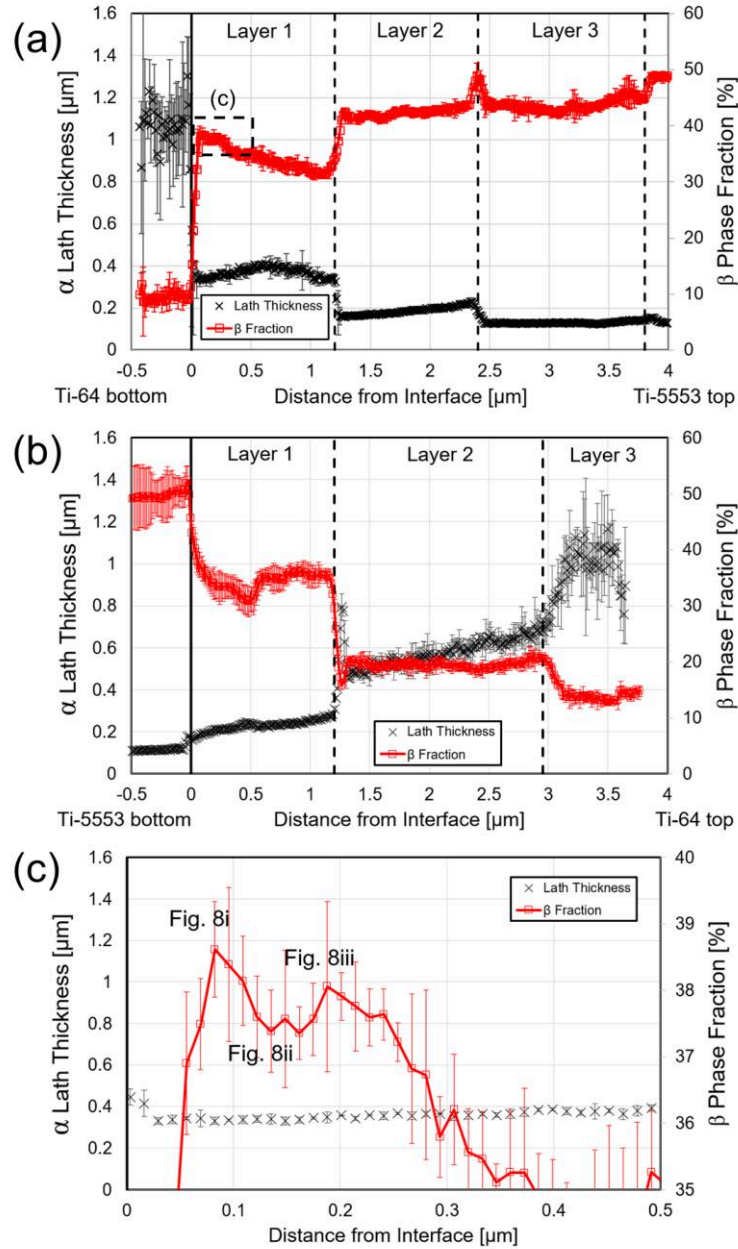
Figure 12. Measurements of the average α lath thickness and β-phase volume fractions across (a) the Ti-64 → Ti-5553 and (b) Ti-5553 → Ti-64 transitions. (c) shows the area highlighted in (a) at higher magnification, which correlates to the region of β-phase instability shown in the EBSD map in Fig. 8a i-iii.

Finally, Fig. 12 further confirms that the α lath size was influenced by the temperature gradients experienced during WAAM deposition as well as the local composition. In Ti-64 WAAM builds, this typically leads to a 'saw-wave' coarsening pattern within the HAZ bands in the build-height (ND) direction [26], [57], [58]. To date, the microstructure homogeneity of monolithic Ti-5553 WAAM builds has not been quantitatively characterised in such detail. Nevertheless, the α lath thickness found across the Ti-64 ↔ Ti-5553 alloy transitions would also be expected to be influenced by thermal gradients caused by the periodic passage of the heat source. Although it was difficult to unambiguously separate such thermal effects from the stronger influence of the compositional gradients, variations in the α lath size were observed that could not be attributed to local composition

fluctuations. For example, in the Ti-5553 → Ti-64 transition distance profile (Fig. 12b), there is a steady increase in α lath size across the second layer, but a sudden peak occurs at the boundary with the third layer, where there is no sudden change in composition; as shown in the EPMA and EDS maps in Fig. 5d and 11d-e, which suggests it was caused by a higher peak temperature experienced during the local thermal history.

4. Discussion

The EPMA results showed that, when building tailored components with the WAAM process, extensive long-range chemical mixing can be expected during the transition between two different titanium alloys. This occurred in a stepwise exponential profile normal to the added layers (e.g. Fig. 5a-b), caused by re-melting, dilution, and mixing in the melt pool, with short-range and steep composition gradients close to the fusion boundary for each new layer (e.g. Fig. 8d-e and Fig. 11d-e). In the alloy combination studied, the change in composition across the alloy transitions had surprisingly little effect on the parent β-grain structure that formed during solidification, which continued to develop as coarse columnar grains that regrew epitaxially from the fusion boundary uninterrupted up through each new layer. This probably occurred because the solidification conditions were too far away from the columnar to equiaxed transition (CET) boundary in both alloys [59], in terms of the solidification front growth rate (R) relative to the liquid thermal gradient (G_L), to see any influence of changes in the partition coefficients, and growth restriction factor (Q) [22], [23] on the primary grain structure. However, the effect of greater solute partitioning in the Ti-5553 alloy was apparent from the observation of the formation of a skin of finer β grains on the sample surfaces, and this situation might therefore be expected to change if the process parameters were modified to reduce the G_L/R ratio [59]. In contrast, the alloy-alloy transition composition profiles strongly influenced the transformation microstructure seen for the α phase, though their effect on the parent β-phase stability, β → α transformation kinetics, and reaction sequence, was not symmetric; i.e. the α microstructure gradient seen when transitioning from Ti-64 → Ti-5553 was significantly different when performed in the reverse order.

4.1 Mixing and Dilution

The long range, stepped, concentration profiles seen across the dissimilar alloy-alloy layer transitions in Fig. 5 can be attributed to liquid phase mixing of solute in the melt pool in each deposition track between the new added wire and the remelted volume, driven by convection, which is subsequently trapped during solidification. In comparison, solid-state diffusion distances, estimated by a simple $\sqrt{Dt}$ [60] calculation using the slowest (Mo) and fastest (Al) elements present, for a representative rapid AM thermal cycle near the melting temperature of Ti-64 (~1500°C [20], t ~ 5 s), are only ~ 0.7 – 2.2 μm, which is over three orders of magnitude smaller than the width of the transition regions in Fig. 5. The composition steps also coincided with the average layer height in the alloy-alloy transition regions, which were ~1.35 mm for Ti-64 → Ti-5553 and ~1.25 mm for Ti-5553 → Ti-64, under the deposition parameters used. In WAAM, with a plasma-arc heat source, the standard process parameters used in this initial study have been optimised to avoid lack of fusion defects, which requires a substantial remelt depth of ~0.7 mm. This results in dilution levels of the newly added material, by the previous layer, in the range of 50 – 70% [34], [35], [61]. This large dilution level has also been previously demonstrated to cause substantial chemical mixing when depositing alternate melt-track alloy-alloy composite (AAC) samples with the WAAM process [5]. For the configuration studied, where new layers of a dissimilar alloy are added onto a previously deposited substrate by changing the feed wire, the effect of dilution on an element's concentration (if it is not present in the new alloy), $C_{x,n}$, through the alloy-alloy transition, can be simply predicted using the relationship:

$$C_{x,n} = C_{x,0}[f_d]^n \qquad\qquad \text{(equation 1)}$$

where $C_{x,0}$ is an element's initial concentration in the base layer, f_d is the fractional dilution of the new alloy added, and n is the layer number. This function is also illustrated in Fig. 13 for different dilution ratios.
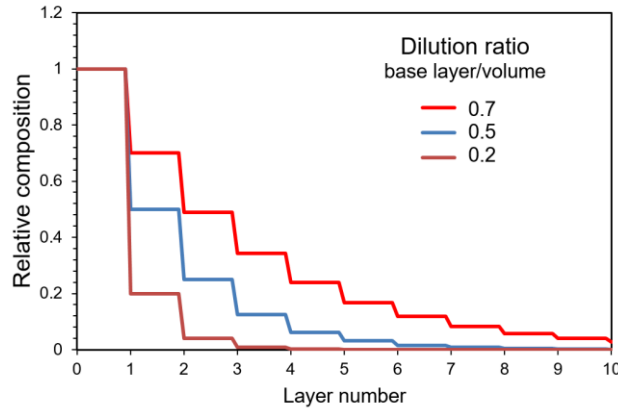

Figure 13. The theoretical composition profile of an alloy element through multiple added layers of a dissimilar alloy wire with different dilution ratios.

Using, Eq. (1) and the mean layer compositions for each step in Table 2, the average dilution can be estimated when transitioning from Ti-64 → Ti-5553 as ~55%, and 45%, for Ti-5553 → Ti-64. The difference between these ratios, which occurred even though constant processing parameters were maintained, resulted from a slightly greater level of remelting when depositing Ti-64 on Ti-5553. This arose because of the effect of the alloys' different physical properties on the remelt depth, due to complex interactions arising between the heat flow, arc pressure, bead profiles and melt-pool liquid circulation. For example, Ti-5553 has a 30% lower thermal conductivity and heat capacity than Ti-64 [62].

This difference in dilution ratio contributed modestly to a greater absolute change in the molybdenum equivalence for the Ti-64 → Ti-5553 transition, relative to the Ti-5553 → Ti-64 transition, of $\Delta Mo_{eq} = 7$ and 4.9, respectively, and similarly also contributed to the different respective β-phase fraction changes for the first alternative alloy added layers of 23.3% and 15%, when reversing the deposition sequence (Table 2). Furthermore, due to the liquid circulation in the melt pool, the first dissimilar alloy wire layer deposited is diluted by the substrate and elements in the remelted prior layer are mixed throughout the new fusion zone, so that during deposition of the next layer they are again diluted by the new alloy wire, though with a lower starting concentration. As this process is repeated, elements present in the base alloy substrate can therefore be carried forwards through many subsequent layers added with the new alloy, as demonstrated in Fig. 13, at a rate of decay that is dependent on the dilution level. This simple model shows that with a large remelt depth – giving a high new dilution ratio of 70% – the substrate elements can be carried forwards over more than 10 added layers, but a smaller remelt depth, producing a low dilution of 20%, would result in a much narrower transition, and the concentration of alloying elements present in the base alloy would decay to very low levels beyond the third layer. Therefore, in dissimilar alloy builds produced with a moving melt pool AM process, a stepped interface is inevitable, and the width of the transition region can be pre-determined by intelligent control of the WAAM deposition process parameters. For example, by using an alternative heat source, such as GMAW-cold metal transfer (CMT), much lower levels of new metal dilution could be achieved (~20%) which would lead to a much sharper interface.

In addition, although mixing between the previous and new melt tracks appears to be efficient in WAAM due to the melt pool circulation, which is driven primarily by Marangoni and arc force convection [35], a liquid boundary layer was still apparent in the composition profile near the fusion boundary for each added layer. This created a steep concentration gradient of the order of ~50 μm wide between each composition step, which strongly influenced the α microstructure and can be seen

enlarged in Fig. 5c-d and in the higher resolution EDS data in Fig. 8 and 11. The width of these fusion boundary composition gradients, though narrower, is again still significantly greater than expected for solid state diffusion. Furthermore, plumes of the remelted substrate alloy, smeared out by liquid shear from convection [5], did not always fully dissipate in the melt pool, which led to some local variation in the composition within each layer step (e.g. Fig. 5 and 8) and the transformation microstructure seen across the transition interface.

4.2 Transformation Microstructures

The factors that affect the local transformation microstructure across the alloy-alloy transition layers can be broadly separated into β parent-phase compositional and thermal history influences. As noted above, prior to transformation, the frozen parent β-phase solid solution composition varies primarily as a step function normal to the added layers, with steep local gradients at each fusion boundary, and some superimposed less severe fluctuations due to incomplete mixing. In addition, in an AM process, after solidification freezes the β-phase chemistry, non-uniform reheating of the deposited material occurs due to the thermal gradients generated below the moving heat source as more melt tracks are added. This results in each volume of material experiencing multiple rapid thermal cycles with a diminishing peak temperature, and heating and cooling rates. The local chemistry strongly affects the local stability of the β phase and the β-transus temperature, but also the transformation kinetics and decomposition pathway [14], [20], whereas the complex thermal conditions include rapid cooling from above the β transus to multiple short reheating cycles with the peak temperatures, ranging from the far-field background temperature to the material's melting point. However, here, because the samples were studied after steady state had been achieved (i.e. after multiple layers had been deposited) and in titanium alloys there is a high sensitivity to chemistry, the composition gradients appear to have dominated the observed microstructure variation.

Under WAAM cooling rate conditions (which are of the order of 30°C s^{-1} [26]) in the baseline Ti-64 alloy, as the temperature first drops below the β transus, the α phase will nucleate both on the β GBs, to produce allotriomorphs and singe-variant α colonies, as well as within the β grains as high-aspect-ratio laths in multi-variant colonies with an interlocking basketweave morphology [36], [46]. This microstructure can also coarsen during subsequent thermal cycling below the β transus if the peak temperature rises to be in the range of the β approach curve (i.e. between ~800 – 1000°C [26], [57], [58]) to form HAZ bands. In contrast, β-stabilised alloys like Ti-5553 have much lower quench sensitivity and will not transform directly to α at these high cooling rates [32]. In addition, during conventional sub-transus heat treatments, a Ti-5553 metastable β-phase solid solution can decompose by multiple transition-phase pathways, involving: spinodal decomposition, the formation of the ω phase by a diffusionless transformation, and the more recently reported disordered and ordered orthorhombic phases O″ and O′, which can affect the subsequent nucleation of α and refine its distribution [31], [63]–[65]. However, these transition phases have a relatively low solvus temperatures (e.g. ~250°C for O′) and have only been found to influence the precipitation of α at much lower heating rates (in WAAM the heating rate is ~500° s^{-1} [26]), or during far longer low temperature heat treatment times than experienced in an AM process [30], [65]. Perhaps more relevant to the rapid heating rate (short thermal cycle) AM thermal conditions is that, in quenching experiments, it has been claimed [66] that α can also nucleate directly from β with a high efficiency, via a psuedo-spinodal mechanism, at relatively short ageing times (e.g. 15 minutes at 600°C) without the requirement for heterogeneous nucleation sites such as dislocations, or the simultaneous appearance of grain boundary α. Whereas, in the range ~650°C to the β transus (~850°C [14], [25], [28]), α precipitates form more coarsely on β GBs and at dislocations within the matrix [66]. Although we do not have any independent evidence to verify this proposed pseudo-spinodal nucleation mechanism, a similar high homogeneous density of α precipitates has been seen here after deposition within the large β grains in the Ti-5553 base layers (e.g. Fig. 6).

As no further phases are expected at intermediate compositions in the dissimilar Ti-64 – Ti-5553 alloy system, in the alloy transitions, the microstructures would be expected to gradate between that of 'pure' Ti-64 to that of Ti-5553. However, when transitioning towards Ti-5553, the β-transus temperature will reduce and the diffusional transformation kinetics will also diminish due to the lower transformation temperature and diffusivity of molybdenum. Conversely, on moving from Ti-5553 to Ti-64, the opposite will occur. Therefore, if the concentration gradients are sufficiently steep for neighbouring α colony nucleation events to interact, the transformation behaviour need not be symmetric, as the sequence of nucleation will be kinetically dependent. For example, when comparing the transformation microstructures seen across the two alloy-alloy transitions sequences, the Ti-64 → Ti-5553 transition produced an abrupt morphological change in the α lamellae, as the Mo_{eq} index and β-phase fraction increased (Fig. 7), but the Ti-5553 → Ti-64 transition gradient exhibited a more progressive change in α (Fig. 9), with only an increase in size seen in the α precipitates across the first added Ti-64 layer (Fig. 10 and 11).

The abrupt α-lath scale and morphological changes seen in the Ti-64 → Ti-5553 transition when the first Ti-5553 rich layer was added resulted in an intermediate bimodal α lath size distribution (Fig. 6 and 7). This occurred because of the transition between two overlapping nucleation sequences that took place as the β-transus temperature deceased and the α transformation kinetics were progressively inhibited. Firstly, starting from the Ti-64 fusion boundary, as the β-phase stability increases when adding Ti-5553, the conventional nucleation of α seen in a Ti-64 alloy during cooling from above the β transus in the WAAM thermal cycle becomes more difficult, because the temperature required to maintain the same undercooling and diffusivity will first decrease and then cease. As a result, primary α laths that have nucleated further towards the Ti-64 rich side, that form variants which are favourably aligned with respect to their principle growth direction relative to the concentration gradient, will continue to grow unimpeded into the metastable β-phase solid solution (centre of Fig. 8g) and the further infilling by autocatalytic nucleation of similarly aligned variants that is normally seen in a Ti-64 alloy as the temperature falls [56] (seen at the bottom of Fig. 8g) also does not appear to take place.

However, the retained β supersaturated matrix will remain highly unstable, and try to precipitate more α as the temperature drops sufficiently to increase the undercooling for further nucleation, or in subsequent heating cycles. The fact that the second distribution of α is much finer in scale and appears very similar to the multi-variant clusters classically seen in the Ti-5553 parent alloy [30], which do not form during cooling from above the β-transus temperature under WAAM conditions [66], however, suggests these fine α laths are precipitated in a subsequent heating cycle where the peak temperature must be close to the 'nose' in the α nucleation curve to allow precipitation in such short time scales. According to Cotton *et al.*, the nose of the α nucleation curve is in the range of 600 – 800°C [14], [32], which is also similar to the temperature range for direct, rapid nucleation of α discussed by Nag *et al.* [66].

On moving across the Ti-64 → Ti-5553 transition, with a further increase in the concentration of β-stabilising elements, this second finer distribution of α precipitates goes on to dominate, as the nucleation of α seen during cooling on the Ti-64 side becomes inhibited and the precipitates become smaller in size as more layers are added, and the parent β phase further increases in stability. This continued reduction in the α precipitate size as the molybdenum content continues to increase occurs simply because, as the β-transus temperature reduces, the equivalent undercooling for nucleation will occur at a lower temperature and diffusivity will therefore reduce, so that the soft impingement diffusion field of the growing α precipitates diminishes more rapidly than their nucleation rate [67].

In comparison, the more progressive microstructure change seen in the reverse Ti-5553 → Ti-64 transition sequence occurs primarily because the Ti-5553 alloy does not appear to occupy a position in the β-phase stability composition space where α nucleation is as sensitive to the dilution of the β-

stabilising elements as when the reverse occurs to Ti-64. Within the first Ti-5553 layers that are alloyed with Ti-64, the β phase thus appears to be still sufficiently stable to avoid transformation during cooling, and precipitation occurs only during subsequent reheating cycles that achieve peak temperatures close to the nose in the α transformation curve, with respect to the local composition. As a result, the microstructure simply coarsens without any morphological change, following the composition gradient with a 'smoother' transition as the β-transus temperature and diffusion rate of the partitioning elements increase, which increases the growth rate relative to the nucleation rate of the α precipitates. In addition, as more layers are added with the Ti-64 wire, because of the exponential dilution behaviour shown in Fig. 13, the composition where the nucleation mechanism changes to that of the baseline Ti-64 alloy is approached much more slowly than when the reverse occurs.

Because of the high sensitivity of the transformation microstructure to composition, local regions of variance in the α lath size, aspect ratio, and phase fractions were noted across the alloy-alloy transitions. Therefore, to explore further how consistent the microstructure transitions described above might be expected to be across a larger scale component, an 8 mm wide EBSD and simultaneous EDS map was obtained, as shown in Fig. 14. When observed over this large interface length, the phase map in Fig. 14a revealed a heterogeneous distribution of areas with different α and β phase fractions laterally across the alloy-alloy transition bands that varied from 100 – 450 μm in thickness. This variation in β stabilisation seen across the transition layers arises from incomplete mixing of liquid shear layers rich in the remelted Ti-64 substrate with the Ti-5553-rich melt pool [5]. The related composition variation is, unfortunately, not obvious in the EDS maps in Fig. 14c-d, since this analysis technique is not as sensitive as EPMA. In addition, in Fig. 14, layers of α can be seen to extend up the higher angle columnar β-grain boundaries that are aligned parallel to the compositional gradient, which clearly provide preferential nucleation conditions for GB α colonies [68], [69]. Overall, this suggests that even quite low variance in the β-stabilising element solute levels (relative to the composition of Ti-64) caused by incomplete mixing, can have a strong effect on the phase fractions and cause significant lateral microstructural variation across an alloy-alloy transition interface that may impact its mechanical performance. The micro-plasticity behaviour in the transition regions is expected to be heterogeneous and complex, and so will be the subject of a future publication.

Finally, it should be noted that the microstructure heterogeneities caused by incomplete solute mixing and the cyclical heating inherent to an AM process could be improved by post-build heat treatments, such β as solutionisation – where the material is heat treated just above, or slightly below, the β transus of the Ti-64 β transus (~980°C), to fully solutionise and homogenise the Ti-5553 alloy and reduce the steep fusion-boundary-layer concentration gradients. When combined with subsequent cooling at a controlled rate, this can also 'reset' the titanium alloy microstructures and, if combined with ageing heat treatments, the properties could then be better tailored to a desired application. For example, β solutionisation followed with a cooling rate of $> 0.1°C \ s^{-1}$ [32] will be sufficient to repress any nucleation of α phase in the Ti-5553 material and will result in a more damage tolerant, coarser α lamellar Ti-64 microstructure [70]. Ti-64 is also relatively insensitive to heat treatments below 700 °C and a subsequent ageing heat treatment could, therefore, also be applied to optimise the desired higher strength and toughness combination possible with the Ti-5553 alloy [25] (which will also be explored in a future publication). Thus, more precisely tailored materials could be readily produced by exploiting both a pre-selected interface transition microstructure gradient, by controlling the dilution level during AM, and using post-build heat treatments to achieve an excellent combination of 'designed' site-specific high strength and damage tolerance properties within a single component.
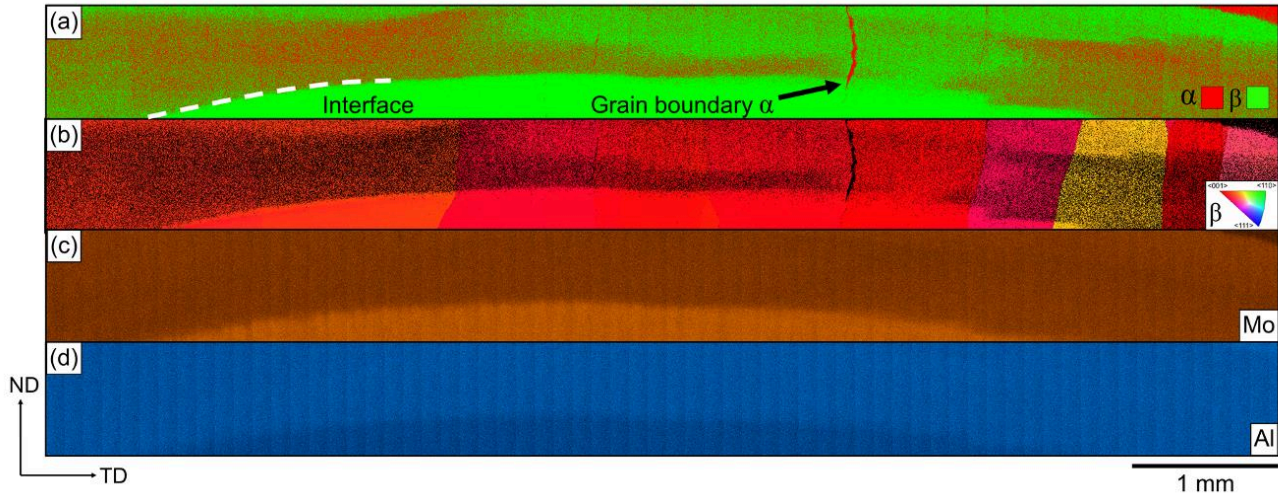
Figure 14. EBSD and EDS maps showing the heterogeneous microstructure across the Ti-5553→Ti-64 interface: (a) EBSD phase map, (b) β-phase inverse pole figure orientation map relative to ND, and (d) EDS Mo and (e) Al maps. Note: these maps were acquired with a higher current and lower step size than those in Fig. 11, so the finer α laths (especially in the pure Ti-5553 section) are less well indexed.

6. Conclusions

The extent and distribution of chemical mixing that occurs across the transition between two high-performance dissimilar titanium alloys, Ti-5553 and Ti-64, has been studied, when producing tailored components by the WAAM process. The consequences of the resultant chemical gradients on the subsequent microstructure and the effect of the alloy addition sequence have also been investigated. It has been shown that extensive chemical mixing can be expected during the transition between two different titanium alloys in a fusion (melt-pool) AM process. This resulted in a long-range, stepwise, exponential decay composition profile, normal to the added layers, that is caused by remelting, dilution, and convective mixing in the melt pool between the prior and new alloy, with steep composition gradients seen within liquid-boundary layers at the fusion boundary of each added layer.

In the alloy combination studied, the change in composition had little apparent effect on the β-grain structure that formed during solidification, which continued uninterrupted through each new layer. In contrast, the alloy-alloy composition profiles dramatically influenced the transformation microstructure seen for the α phase, through their strong effect on the parent β-phase stability and the β → α transformation kinetics and reaction sequence.

The α microstructure gradient seen when transitioning from Ti-64 → Ti-5553 was more abrupt, compared to when depositing the two alloys in the reverse order (i.e. Ti-5553 → Ti-64). In the former case, the transformation behaviour of Ti-64 under WAAM thermal conditions appears to be more sensitive to the effect of β-stabilising elements than when Ti-5553 is diluted by Ti-64. This is because, with the high cooling rates in a WAAM process, greater stabilisation of the β phase readily suppresses α nucleation when cooling through the β transus, to be replaced by much finer-scale α laths generated by precipitation during subsequent reheating cycles.

It is also shown that the width of the alloy-alloy interface transition layer can be described by a simple dilution law, offering the ability to design α transformation microstructure gradients by controlling the level of remelting in the WAAM process, with the potential to make much sharper interfaces by employing alternative technologies (e.g. such as CMT).

Finally, it is noted that the properties of the Ti-64 ↔ Ti-5553 alloy combination studied can be further readily 'tailored' by applying post-build heat treatments that exploit the lower solution treatment and ageing temperatures of Ti-5553, to optimise the site specific strength and damage tolerance obtainable within a single titanium AM component.

Acknowledgements

Data Availability

The raw/processed data required to reproduce these findings cannot be shared at this time due to technical or time limitations.

References

[1] T. Duda and L. V. Raghavan, "3D Metal Printing Technology," *IFAC-PapersOnLine*, vol. 49, no. 29, pp. 103–110, 2016, doi: 10.1016/j.ifacol.2016.11.111.

[2] W. J. Sames, F. A. List, S. Pannala, R. R. Dehoff, and S. S. Babu, "The metallurgy and processing science of metal additive manufacturing," *Int. Mater. Rev.*, vol. 61, no. 5, pp. 315–360, 2016, doi: 10.1080/09506608.2015.1116649.

[3] F. Martina, J. Mehnen, S. W. Williams, P. A. Colegrove, and F. Wang, "Investigation of the benefits of plasma deposition for the additive layer manufacture of Ti-6Al-4V," *J. Mater. Process. Technol.*, vol. 212, no. 6, pp. 1377–1386, 2012, doi: 10.1016/j.jmatprotec.2012.02.002.

[4] G. Marinelli, F. Martina, S. Ganguly, and S. Williams, "Development of Wire + Arc additive manufacture for the production of large-scale unalloyed tungsten components," *Int. J. Refract. Met. Hard Mater.*, vol. 82, no. February, pp. 329–335, 2019, doi: 10.1016/j.ijrmhm.2019.05.009.

[5] A. E. Davis *et al.*, "Mechanical performance and microstructural characterisation of titanium alloy-alloy composites built by wire-arc additive manufacture," *Mater. Sci. Eng. A*, vol. 765, 2019, doi: 10.1016/j.msea.2019.138289.

[6] R. Banerjee, P. C. Collins, D. Bhattacharyya, S. Banerjee, and H. L. Fraser, "Microstructural evolution in laser deposited compositionally graded α/β titanium-vanadium alloys," *Acta Mater.*, vol. 51, no. 11, pp. 3277–3292, 2003, doi: 10.1016/S1359-6454(03)00158-7.

[7] C. Schneider-Maunoury, L. Weiss, D. Boisselier, and P. Laheurte, "Crystallographic analysis of functionally graded titanium-molybdenum alloys with DED-CLAD® process," *Procedia CIRP*, vol. 74, pp. 180–183, 2018, doi: 10.1016/j.procir.2018.08.089.

[8] B. Onuike and A. Bandyopadhyay, "Additive manufacturing of Inconel 718 – Ti6Al4V bimetallic structures," *Addit. Manuf.*, vol. 22, no. June, pp. 844–851, 2018, doi: 10.1016/j.addma.2018.06.025.

[9] D. C. Hofmann *et al.*, "Developing gradient metal alloys through radial deposition additive manufacturing," *Sci. Rep.*, vol. 4, 2014, doi: 10.1038/srep05357.

[10] B. Vamsi Krishna, W. Xue, S. Bose, and A. Bandyopadhyay, "Functionally graded Co-Cr-Mo

coating on Ti-6Al-4V alloy structures," *Acta Biomater.*, vol. 4, no. 3, pp. 697–706, 2008, doi: 10.1016/j.actbio.2007.10.005.

[11]   J. Wang *et al.*, "Characterization of wire arc additively manufactured titanium aluminide functionally graded material: Microstructure, mechanical properties and oxidation behaviour," *Mater. Sci. Eng. A*, vol. 734, no. May, pp. 110–119, 2018, doi: 10.1016/j.msea.2018.07.097.

[12]   E. Hernández-Nava, P. Mahoney, C. J. Smith, J. Donoghue, I. Todd, and S. Tammas-Williams, "Additive manufacturing titanium components with isotropic or graded properties by hybrid electron beam melting/hot isostatic pressing powder processing," *Sci. Rep.*, vol. 9, no. 1, pp. 1–11, 2019, doi: 10.1038/s41598-019-40722-3.

[13]   J. J. Pope, E. L. Calvert, N. S. Weston, and M. Jackson, "FAST-DB: A novel solid-state approach for diffusion bonding dissimilar titanium alloy powders for next generation critical components," *J. Mater. Process. Technol.*, vol. 269, no. June 2018, pp. 200–207, 2019, doi: 10.1016/j.jmatprotec.2019.02.011.

[14]   J. D. Cotton *et al.*, "State of the Art in Beta Titanium Alloys for Airframe Applications," *Jom*, vol. 67, no. 6, pp. 1281–1303, 2015, doi: 10.1007/s11837-015-1442-4.

[15]   C. Hicks, T. Konkova, and P. Blackwell, "Influence of laser power and powder feed rate on the microstructure evolution of laser metal deposited Ti-5553 on forged substrates," *Mater. Charact.*, vol. 170, no. February, p. 110675, 2020, doi: 10.1016/j.matchar.2020.110675.

[16]   C. Qiu, G. A. Ravi, and M. M. Attallah, "Microstructural control during direct laser deposition of a β-titanium alloy," *Mater. Des.*, vol. 81, pp. 21–30, 2015, doi: 10.1016/j.matdes.2015.05.031.

[17]   F. Wang *et al.*, "Effect of heat treatment on microstructures and tensile properties of TA19 alloy fabricated by laser metal deposition," *Mater. Sci. Eng. A*, vol. 782, no. March, p. 139284, 2020, doi: 10.1016/j.msea.2020.139284.

[18]   Y. Y. Zhu, H. B. Tang, Z. Li, C. Xu, and B. He, "Solidification behavior and grain morphology of laser additive manufacturing titanium alloys," *J. Alloys Compd.*, vol. 777, pp. 712–716, 2019, doi: 10.1016/j.jallcom.2018.11.055.

[19]   C. H. Ng, M. J. Bermingham, D. Kent, and M. S. Dargusch, "High stability and high strength β-titanium alloys for additive manufacturing," *Mater. Sci. Eng. A*, vol. 816, no. December 2020, 2021, doi: 10.1016/j.msea.2021.141326.

[20]   G. Lütjering and J. C. Williams, *Titanium*. Springer, 2007.

[21]   T. W. Duerig and J. C. Williams, "Overview: microstructure and properties of beta titanium alloys," *Beta Titan. Alloy. 1980's*, pp. 19–67, 1984.

[22]   M. J. Bermingham, S. D. McDonald, M. S. Dargusch, and D. H. St.John, "Grain-refinement mechanisms in titanium alloys," *J. Mater. Res.*, vol. 23, no. 1, pp. 97–104, 2008, doi: 10.1557/jmr.2008.0002.

[23]   M. J. Bermingham, S. D. McDonald, D. H. StJohn, and M. S. Dargusch, "Beryllium as a grain refiner in titanium alloys," *J. Alloys Compd.*, vol. 481, no. 1–2, pp. 20–23, 2009, doi: 10.1016/j.jallcom.2009.03.016.

[24]   T. Lyman, *Atlas of Microstructures of Industrial Alloys*. American Society for Metals, 1972.

[25]   ASM International, *Materials Properties Handbook: Titanium Alloys*. Materials Park, OH., 1994.

[26]   A. Ho, H. Zhao, J. W. Fellowes, F. Martina, A. E. Davis, and P. B. Prangnell, "On the origin of microstructural banding in Ti-6Al4V wire-arc based high deposition rate additive manufacturing," *Acta Mater.*, vol. 166, pp. 306–323, 2019, doi: 10.1016/j.actamat.2018.12.038.

[27]   A. Kumar, T. Jayakumar, B. Raj, and D. Banerjee, "A new methodology for identification of β-transus temperature in α + β and β titanium alloys using ultrasonic velocity measurement," *Philos. Mag.*, vol. 88, no. 3, pp. 327–338, 2008, doi: 10.1080/14786430701837015.

[28]   J. C. Fanning, "Properties of TIMETAL 555 (Ti-5Al-5Mo-5V-3Cr-0.6Fe)," *J. Mater. Eng. Perform.*, vol. 14, no. 6, pp. 788–791, 2005, doi: 10.1361/105994905X75628.

[29]   C. M. Liu, H. M. Wang, X. J. Tian, H. B. Tang, and D. Liu, "Microstructure and tensile properties of laser melting deposited Ti-5Al-5Mo-5V-1Cr-1Fe near β titanium alloy," *Mater. Sci. Eng. A*, vol. 586, pp. 323–329, 2013, doi: 10.1016/j.msea.2013.08.032.

[30]   S. Nag, R. Banerjee, R. Srinivasan, J. Y. Hwang, M. Harper, and H. L. Fraser, "ω-Assisted

nucleation and growth of α precipitates in the Ti-5Al-5Mo-5V-3Cr-0.5Fe β titanium alloy," *Acta Mater.*, vol. 57, no. 7, pp. 2136–2147, 2009, doi: 10.1016/j.actamat.2009.01.007.

[31] N. G. Jones, R. J. Dashwood, M. Jackson, and D. Dye, "β Phase decomposition in Ti-5Al-5Mo-5V-3Cr," *Acta Mater.*, vol. 57, no. 13, pp. 3830–3839, 2009, doi: 10.1016/j.actamat.2009.04.031.

[32] J. D. Cotton *et al.*, "Phase Transformations in Ti-5Al-5Mo-5V-3Cr-0.5Fe," *Proc. Ti-2007 Sci. Technol. Japan Inst. Met.*, 2007.

[33] R. Sahoo and A. Kabir, "Effect of Heat Treatments on Microstructures and Mechanical Properties of Ti-5553 Alloy," in *TMS 2020 149th Annual Meeting & Exhibition Supplemental Proceedings*, 2020, pp. 1799–1807, doi: https://doi.org/10.1007/978-3-030-36296-6_166.

[34] S. Ríos, P. A. Colegrove, F. Martina, and S. W. Williams, "Analytical process model for wire + arc additive manufacturing," *Addit. Manuf.*, vol. 21, no. August 2017, pp. 651–657, 2018, doi: 10.1016/j.addma.2018.04.003.

[35] X. Bai *et al.*, "Numerical analysis of heat transfer and fluid flow in multilayer deposition of PAW-based wire and arc additive manufacturing," *Int. J. Heat Mass Transf.*, vol. 124, pp. 504–516, 2018, doi: 10.1016/j.ijheatmasstransfer.2018.03.085.

[36] A. K. Syed *et al.*, "Effect of deposition strategies on fatigue crack growth behaviour of wire + arc additive manufactured titanium alloy Ti–6Al–4V," *Mater. Sci. Eng. A*, vol. 814, no. January, p. 141194, 2021, doi: 10.1016/j.msea.2021.141194.

[37] A. R. McAndrew *et al.*, "Interpass rolling of Ti-6Al-4V wire + arc additively manufactured features for microstructural refinement," *Addit. Manuf.*, vol. 21, no. March, pp. 340–349, 2018, doi: 10.1016/j.addma.2018.03.006.

[38] S. Zaheeruddin and K. Suganthi, "Image Contrast Enhancement by Homomorphic Filtering based Parametric Fuzzy Transform," in *Procedia Computer Science*, 2019, vol. 165, pp. 166–172, doi: 10.1016/j.procs.2020.01.095.

[39] Otsu and N., "A threshold selection method from gray-level histograms," *IEEE Trans. Syst. Man Cybern.*, vol. 9, no. 1, 1996.

[40] L. Vincent, "Grayscale Area Openings and Closings: their Applications and Efficient Implementation," *EURASIP Work. Math. Morphol. its Appl. to Signal Process.*, 1993.

[41] ASTM, "E 1382-97. Standard Test Methods for Determining Average Grain Size Using Semiautomatic and Automatic Image Analysis," *ASTM Int. Conshohocken, PA, www.astm.org*, 2015, doi: 10.1520/E1382-97R15.

[42] M. White, "ILS Measurement Python Package." .

[43] P. S. Davies, "An investigation of microstructure and texture evolution in the Near-α titanium alloy Timetal 834," University of Sheffield, 2009.

[44] P. S. Davies, B. P. Wynne, W. M. Rainforth, M. J. Thomas, and P. L. Threadgill, "Development of microstructure and crystallographic texture during stationary shoulder friction stir welding of Ti-6Al-4V," *Metall. Mater. Trans. A Phys. Metall. Mater. Sci.*, vol. 42, no. 8, pp. 2278–2289, 2011, doi: 10.1007/s11661-011-0606-2.

[45] J. R. Hönnige *et al.*, "The Effectiveness of Grain Refinement by Machine Hammer Peening in High Deposition Rate Wire-Arc AM Ti-6Al-4V," *Metall. Mater. Trans. A*, vol. 51, pp. 3692–3703, 2020.

[46] F. Wang, S. W. Williams, P. A. Colegrove, and A. A. Antonysamy, "Microstructure and mechanical properties of wire and arc additive manufactured Ti-6Al-4V," *Metall. Mater. Trans. A Phys. Metall. Mater. Sci.*, vol. 44, no. 2, pp. 968–977, 2013, doi: 10.1007/s11661-012-1444-6.

[47] P. Åkerfeldt, M. L. Antti, and R. Pederson, "Influence of microstructure on mechanical properties of laser metal wire-deposited Ti-6Al-4V," *Mater. Sci. Eng. A*, vol. 674, pp. 428–437, 2016, doi: 10.1016/j.msea.2016.07.038.

[48] K. M. Taminger and R. A. Hafley, "Electron Beam Freeform Fabrication for Cost Effective Near-Net Shape Manufacturing," *Spec. Meet. Cost Eff. Manuf. via Net Shape Process. (NATO/RTO AVT-139)*, pp. 16:1–10, 2006.

[49] D. Kovalchuk and O. Ivasishin, *Profile electron beam 3D metal printing*. Elsevier Inc., 2019.

[50] L. Neto, S. W. Williams, J. Ding, J. R. Hönnige, and F. Martina, "Mechanical Properties

Enhancement of Additive Manufactured Ti-6Al-4V by Machine Hammer Peening," *Adv. Surf. Enhanc. 1st Int. Conf. Adv. Surf. Enhanc.*, vol. 1, pp. 121–132, 2020, doi: 10.1007/978-981-15-0054-1.

[51] D. Lunt *et al.,* "The effect of loading direction on strain localisation in wire arc additively manufactured Ti–6Al–4V," *Mater. Sci. Eng. A*, vol. 788, p. 139608, 2020, doi: 10.1016/j.msea.2020.139608.

[52] P. A. Kobryn and S. L. Semiatin, "The laser additive manufacture of Ti-6Al-4V," *Jom*, vol. 53, no. 9, pp. 40–42, 2001, doi: 10.1007/s11837-001-0068-x.

[53] J. Donoghue, A. A. Antonysamy, F. Martina, P. A. Colegrove, S. W. Williams, and P. B. Prangnell, "The effectiveness of combining rolling deformation with Wire-Arc Additive Manufacture on β-grain refinement and texture modification in Ti-6Al-4V," *Mater. Charact.*, vol. 114, pp. 103–114, 2016, doi: 10.1016/j.matchar.2016.02.001.

[54] J. Wang *et al.*, "Grain morphology evolution and texture characterization of wire and arc additive manufactured Ti-6Al-4V," *J. Alloys Compd.*, vol. 768, pp. 97–113, 2018, doi: 10.1016/j.jallcom.2018.07.235.

[55] A. E. Davis, J. R. Kennedy, J. Ding, and P. B. Prangnell, "The effect of processing parameters on rapid-heating β recrystallization in inter-pass deformed Ti-6Al-4V wire-arc additive manufacturing," *Mater. Charact.*, vol. 163, no. February, 2020, doi: 10.1016/j.matchar.2020.110298.

[56] A. E. Davis, J. Donoghue, J. R. Kennedy, N. Byres, and P. B. Prangnell, "In-Situ Observation of Single Variant α Colony Formation in Ti-6Al-4V," *Under Rev.*, 2021.

[57] S. M. Kelly and S. L. Kampe, "Microstructural evolution in laser-deposited multilayer Ti-6Al-4V builds: Part I. Microstructure Characterization," *Metall. Mater. Trans. A*, vol. 35 A, no. 6, pp. 1861–1867, 2004, doi: 10.1007/s11661-004-0095-7.

[58] S. M. Kelly and S. L. Kampe, "Microstructural Evolution in Laser-Deposited Multilayer Ti-6Al-4V Builds: Part II. Thermal Modeling," *Metall. Mater. Trans. A*, vol. 35A, no. June, pp. 1869–1879, 2004.

[59] P. A. Kobryn and S. L. Semiatin, "Microstructure and texture evolution during solidification processing of Ti-6A1-4V," *J. Mater. Process. Technol.*, vol. 135, no. 2-3 SPEC., pp. 330–339, 2003, doi: 10.1016/S0924-0136(02)00865-8.

[60] D. A. Porter and K. E. Easterling, *Phase Transformations in Metals and Alloys*, vol. 3. 1992.

[61] A. Caballero, "Dilution study Ti-6Al-4V LAMP project," 2018.

[62] M. Nouari and H. Makich, "On the Physics of Machining Titanium Alloys: Interactions between Cutting Parameters, Microstructure and Tool Wear," *Metals (Basel).*, vol. 4, no. 3, pp. 335–358, 2014, doi: 10.3390/met4030335.

[63] P. Barriobero-Vila, G. Requena, S. Schwarz, F. Warchomicka, and T. Buslaps, "Influence of phase transformation kinetics on the formation of α in a β-quenched Ti-5Al-5Mo-5V-3Cr-1Zr alloy," *Acta Mater.*, vol. 95, pp. 90–101, 2015, doi: 10.1016/j.actamat.2015.05.008.

[64] Y. Zheng, S. Antonov, Q. Feng, R. Banerjee, D. Banerjee, and H. L. Fraser, "Shuffle-induced modulated structure and heating-induced ordering in the metastable β-titanium alloy, Ti-5Al-5Mo-5V-3Cr," *Scr. Mater.*, vol. 176, pp. 7–11, 2020, doi: 10.1016/j.scriptamat.2019.09.027.

[65] S. Antonov *et al.*, "Nucleation and growth of α phase in a metastable β-Titanium Ti-5Al-5Mo-5V-3Cr alloy: Influence from the nano-scale, ordered-orthorhombic O″ phase and α compositional evolution," *Scr. Mater.*, vol. 194, pp. 1–5, 2021, doi: 10.1016/j.scriptamat.2020.113672.

[66] S. Nag *et al.*, "Non-classical homogeneous precipitation mediated by compositional fluctuations in titanium alloys," *Acta Mater.*, vol. 60, no. 18, pp. 6247–6256, 2012, doi: 10.1016/j.actamat.2012.07.033.

[67] J. W. Christian, *The Theory of Transformations in Metals and Alloys*. Oxford: Pergamon Press, 1975.

[68] N. Stanford and P. S. Bate, "Crystallographic variant selection in Ti-6Al-4V," *Acta Mater.*, vol. 52, no. 17, pp. 5215–5224, 2004, doi: 10.1016/j.actamat.2004.07.034.

[69] D. Bhattacharyya, G. B. Viswanathan, R. Denkenberger, D. Furrer, and H. L. Fraser, "The role

of crystallographic and geometrical relationships between α and β phases in an α/β titanium alloy," *Acta Mater.*, vol. 51, no. 16, pp. 4679–4691, 2003, doi: 10.1016/S1359-6454(03)00179-4.

[70]   R. K. Nalla, B. L. Boyce, J. P. Campbell, J. O. Peters, and R. O. Ritchie, "Influence of microstructure on high-cycle fatigue of Ti-6Al-4V: bimodal vs. lamellar structures," *Metall. Mater. Trans. A*, vol. 33A, pp. 899–918, 2002, doi: 10.13140/RG.2.1.3668.1201.

Declaration of interests

☐ The authors declare that they have no known competing financial interests or personal relationships that could have appeared to influence the work reported in this paper.

☐The authors declare the following financial interests/personal relationships which may be considered as potential competing interests:

No interests to declare.

- Chemical mixing of Ti-64 & Ti-5553 deposited using the WAAM process was studied.
- Microstructure gradients of the two alloys were also investigated.
- Alloy mixing occurred in a stepwise manner across 3-4 deposited layers.
- Deposition order of the alloys was shown to affect the α+β microstructure gradient.

2021-11-03

Microstructure transition gradients in titanium dissimilar alloy (Ti-5AI-5V-5Mo-3Cr/Ti-6AI-4V) tailored wire-arc additively manufactured components

Kennedy, Jacob R.

Elsevier